THE EFFECT OF INTRINSIC DATASET PROPERTIES ON GENERALIZATION: UNRAVELING LEARNING DIFFERENCES BETWEEN NATURAL AND MEDICAL IMAGES

Nicholas Konz¹, Maciej A. Mazurowski^{1,2,3,4}

- ¹ Department of Electrical and Computer Engineering, ² Department of Radiology,
- ³ Department of Computer Science, ⁴ Department of Biostatistics & Bioinformatics Duke University, NC, USA

{nicholas.konz, maciej.mazurowski}@duke.edu

ABSTRACT

This paper investigates discrepancies in how neural networks learn from different imaging domains, which are commonly overlooked when adopting computer vision techniques from the domain of natural images to other specialized domains such as medical images. Recent works have found that the generalization error of a trained network typically increases with the intrinsic dimension (d_{data}) of its training set. Yet, the steepness of this relationship varies significantly between medical (radiological) and natural imaging domains, with no existing theoretical explanation. We address this gap in knowledge by establishing and empirically validating a generalization scaling law with respect to d_{data} , and propose that the substantial scaling discrepancy between the two considered domains may be at least partially attributed to the higher intrinsic "label sharpness" $(K_{\mathcal{F}})$ of medical imaging datasets, a metric which we propose. Next, we demonstrate an additional benefit of measuring the label sharpness of a training set: it is negatively correlated with the trained model's adversarial robustness, which notably leads to models for medical images having a substantially higher vulnerability to adversarial attack. Finally, we extend our d_{data} formalism to the related metric of learned representation intrinsic dimension (d_{repr}), derive a generalization scaling law with respect to d_{repr} , and show that d_{data} serves as an upper bound for d_{repr} . Our theoretical results are supported by thorough experiments with six models and eleven natural and medical imaging datasets over a range of training set sizes. Our findings offer insights into the influence of intrinsic dataset properties on generalization, representation learning, and robustness in deep neural networks.¹

1 Introduction

There has been recent attention towards how a neural network's ability to generalize to test data relates to the *intrinsic dimension* $d_{\rm data}$ of its training dataset, *i.e.*, the dataset's inherent "complexity" or the minimum degrees of freedom needed to represent it without substantial information loss (Gong et al., 2019). Recent works have found that generalization error typically increases with $d_{\rm data}$, empirically (Pope et al., 2020) or theoretically (Bahri et al., 2021). Such "scaling laws" with respect to intrinsic dataset properties are attractive because they may describe neural network behavior in generality, for different models and/or datasets, allowing for better understanding and predictability of the behavior, capabilities, and challenges of deep learning. However, a recent study (Konz et al., 2022) showed that generalization scaling behavior differs drastically depending on the input image type, *e.g.*, natural or medical images, showing the non-universality of the scaling law and motivating us to consider its relationship to properties of the dataset and imaging domain.²

In this work, we provide theoretical and empirical findings on how measurable intrinsic properties of an image dataset can affect the behavior of a neural network trained on it. We show that certain

¹Code link: https://github.com/mazurowski-lab/intrinsic-properties.

²Here we take "medical" images to refer to radiology images (e.g., x-ray, MRI), the most common type.

dataset properties that differ between imaging domains can lead to discrepancies in behaviors such as generalization ability and adversarial robustness. Our contributions are summarized as follows.

First, we introduce the novel measure of the intrinsic **label sharpness** $(K_{\mathcal{F}})$ of a dataset (defined in Section 3.2). The label sharpness essentially measures how similar images in the dataset can be to each other while still having different labels, and we find that it usually differs noticeably between natural and medical image datasets. We then derive and test a neural network generalization scaling law with respect to dataset intrinsic dimension d_{data} , which includes $K_{\mathcal{F}}$. Our experiments support the derived scaling behavior within each of these two domains, and show a distinct difference in the scaling rate between them. According to our scaling law, this may be due to the measured $K_{\mathcal{F}}$ being typically higher for medical datasets.

Next, we show how a model's adversarial robustness relates to its training set's $K_{\mathcal{F}}$, and show that over a range of attacks, robustness decreases with higher $K_{\mathcal{F}}$. Medical image datasets, which have higher $K_{\mathcal{F}}$, are typically more susceptible to adversarial attack than natural image datasets. Finally, we extend our d_{data} formalism to derive and test a generalization scaling law with respect to the intrinsic dimension of the model's learned representations, d_{repr} , and reconcile the d_{data} and d_{repr} scaling laws to show that d_{data} serves as an approximate upper bound for d_{repr} . We also provide many additional results in the supplementary material, such as a likelihood analysis of our proposed scaling law given observed generalization data, the evaluation of a new dataset in a third domain, an example of a practical application of our findings, and more.

All theoretical results are validated with thorough experiments on six convolutional models and eleven datasets from natural and medical imaging domains over a range of training set sizes. We hope that our work initiates further study into how network behavior differs between imaging domains.

2 RELATED WORKS

We are interested in the scaling of the generalization ability of supervised convolutional neural networks with respect to intrinsic properties of the training set. Other works have also explored generalization scaling with respect to parameter count or training set size for vision or other modalities (Caballero et al., 2023; Kaplan et al., 2020; Hoffmann et al., 2022; Touvron et al., 2023). Note that we model the intrinsic dimension to be constant throughout the dataset's manifold as in Pope et al. (2020); Bahri et al. (2021) for simplicity, as opposed to the recent work of Brown et al. (2023), which we find to be suitable for interpretable scaling laws and dataset properties.

Similar to *dataset* intrinsic dimension scaling (Pope et al., 2020; Bahri et al., 2021; Konz et al., 2022), recent works have also found a monotonic relationship between a network's generalization error and the intrinsic dimension of both the learned hidden layer representations (Ansuini et al., 2019), or some measure of intrinsic dimensionality of the trained model itself (Birdal et al., 2021; Andreeva et al., 2023). In this work, we focus on the former, as the latter model dimensionality measures are typically completely different mathematical objects than the intrinsic dimension of the manifolds of data or representations. Similarly, Kvinge et al. (2023) found a correlation between prompt perplexity and representation intrinsic dimension in Stable Diffusion models.

3 Preliminaries

We consider a binary classification dataset \mathcal{D} of points $x \in \mathbb{R}^n$ with target labels $y = \mathcal{F}(x)$ defined by some unknown function $\mathcal{F}: \mathbb{R}^n \to \{0,1\}$, split into a training set $\mathcal{D}_{\text{train}}$ of size N and test set $\mathcal{D}_{\text{test}}$. The manifold hypothesis (Fefferman et al., 2016) assumes that the input data x lies approximately on some d_{data} -dimensional manifold $\mathcal{M}_{d_{\text{data}}} \subset \mathbb{R}^n$, with $d_{\text{data}} \ll n$. More technically, $\mathcal{M}_{d_{\text{data}}}$ is a metric space such that for all $x \in \mathcal{M}_{d_{\text{data}}}$, there exists some neighborhood U_x of x such that U_x is homeomorphic to $\mathbb{R}^{d_{\text{data}}}$, defined by the standard L_2 distance metric $||\cdot||$.

As in Bahri et al. (2021), we consider over-parameterized (number of parameters $\gg N$) models $f(x):\mathbb{R}^n \to \{0,1\}$, that are "well-trained" and learn to interpolate all training data: $f(x)=\mathcal{F}(x)$ for all $x\in\mathcal{D}_{\mathrm{train}}$. We use a non-negative loss function L, such that L=0 when $f(x)=\mathcal{F}(x)$. Note that we write L as the expected loss over a set of test set points. We assume that \mathcal{F}, f and L are Lipschitz/smooth on $\mathcal{M}_{d_{\mathrm{data}}}$ with respective constants $K_{\mathcal{F}}, K_f$ and K_L . Note that we use

the term "Lipschitz constant" of a function to refer to the smallest value that satisfies the Lipschitz inequality.³ We focus on binary classification as in Pope et al. (2020); Konz et al. (2022), but we note that our results extend naturally to the multi-class case (see Appendix A.1 for more details).

3.1 ESTIMATING DATASET INTRINSIC DIMENSION

Here we introduce two common intrinsic dimension estimators for high-dimensional datasets that we use in our experiments, which have been used in prior works on image datasets (Pope et al., 2020; Konz et al., 2022) and learned representations (Ansuini et al., 2019; Gong et al., 2019).

MLE: The MLE (maximum likelihood estimation) intrinsic dimension estimator (Levina & Bickel, 2004; MacKay & Ghahramani, 2005) works by assuming that the number of datapoints enclosed within some ϵ -ball about some point on $\mathcal{M}_{d_{\text{data}}}$ scales not as $\mathcal{O}(\epsilon^n)$, but $\mathcal{O}(\epsilon^{d_{\text{data}}})$, and then solving for d_{data} with MLE after modeling the data as sampled from a Poisson process. This results in $\hat{d}_{\text{data}} = \left[\frac{1}{N(k-1)}\sum_{i=1}^{N}\sum_{j=1}^{k-1}\log\frac{T_k(x_i)}{T_j(x_i)}\right]^{-1}$, where $T_j(x)$ is the L_2 distance from x to its j^{th} nearest neighbor and k is a hyperparameter; we set k=20 as in Pope et al. (2020); Konz et al. (2022). TwoNN: TwoNN (Facco et al., 2017) is a similar approach that instead relies on the ratio of the first- and second-nearest neighbor distances. We default to using the MLE method for d_{data} estimation as Pope et al. (2020) found it to be more reliable for image data than TwoNN, but we still evaluate with TwoNN for all experiments. Note that these estimators do not use datapoint labels.

3.2 ESTIMATING DATASET LABEL SHARPNESS

Another property of interest is an empirical estimate for the "label sharpness" of a dataset, $K_{\mathcal{F}}$. This measures the extent to which images in the dataset can resemble each other while still having different labels. Formally, $K_{\mathcal{F}}$ is the Lipschitz constant of the ground truth labeling function \mathcal{F} , i.e., the smallest positive $K_{\mathcal{F}}$ that satisfies $K_{\mathcal{F}}||x_1-x_2|| \geq |\mathcal{F}(x_1)-\mathcal{F}(x_2)| = |y_1-y_2|$ for all $x_1,x_2 \sim \mathcal{M}_{d_{\text{data}}}$, where $y_i = \mathcal{F}(x_i) \in \{0,1\}$ is the target label for x_i . We estimate this as

$$\hat{K}_{\mathcal{F}} := \max_{j,k} \left(\frac{|y_j - y_k|}{||x_j - x_k||} \right),\tag{1}$$

computed over all M^2 pairings $((x_j,y_j),(x_k,y_k))$ of some M evenly class-balanced random samples $\{(x_i,y_i)\}_{i=1}^M$ from the dataset \mathcal{D} . We use M=1000 in practice, which we found more than sufficient for a converging estimate, and it takes <1 sec. to compute $\hat{K}_{\mathcal{F}}$. We minimize the effect of trivial dataset-specific factors on $\hat{K}_{\mathcal{F}}$ by linearly normalizing all images to the same range (Sec. 4), and we note that both $\hat{K}_{\mathcal{F}}$ and d_{data} are invariant to image resolution and channel count (Appendix B.1). As the natural image datasets have multiple possible combinations of classes for the binary classification task, we report $\hat{K}_{\mathcal{F}}$ averaged over 25 runs of randomly chosen class pairings.

4 DATASETS, MODELS AND TRAINING

Medical Image Datasets. We conducted our experiments on seven public medical image (radiology) datasets from diverse modalities and anatomies for different binary classification tasks. These are (1) brain MRI glioma detection (BraTS, Menze et al. (2014)); (2) breast MRI cancer detection (DBC, Saha et al. (2018)); (3) prostate MRI cancer risk scoring (Prostate MRI, Sonn et al. (2013)); (4) brain CT hemorrhage detection (RSNA-IH-CT, Flanders et al. (2020)); (5) chest X-ray pleural effusion detection (CheXpert, Irvin et al. (2019)); (6) musculoskeletal X-ray abnormality detection (MURA, Rajpurkar et al. (2017)); and (7) knee X-ray osteoarthritis detection (OAI, Tiulpin et al. (2018)). All dataset preparation and task definition details are provided in Appendix G.

Natural Image Datasets. We also perform our experiments using four common "natural" image classification datasets: **ImageNet** (Deng et al., 2009), **CIFAR10** (Krizhevsky et al., 2009), **SVHN** (Netzer et al., 2011), and **MNIST** (Deng, 2012).

 $^{^3}$ A subtlety here is that our Lipschitz assumptions only involve pairs of neighboring datapoints sampled from the true data manifold $\mathcal{M}_{d_{\mathrm{data}}}$; adversarially-perturbed images (Goodfellow et al., 2015) are not included.

For each dataset, we create training sets of size $N \in \{500, 750, 1000, 1250, 1500, 1750\}$, along with a test set of 750 examples. These splits are randomly sampled with even class-balancing from their respective base datasets. For the natural image datasets we choose two random classes (different for each experiment) to define the binary classification task, and all results are averaged over five runs using different class pairs. Images are resized to 224×224 and normalized linearly to [0,1].

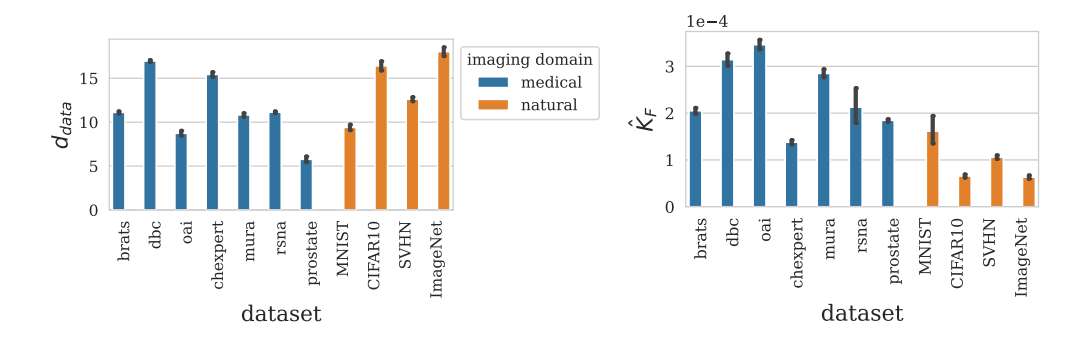


Figure 1: Measured intrinsic dimension ($d_{\rm data}$, left) and label sharpnesses ($\hat{K}_{\mathcal{F}}$, right) of the natural (orange) and medical (blue) image datasets which we analyze (Sec. 4). $\hat{K}_{\mathcal{F}}$ is typically higher for the medical datasets. $d_{\rm data}$ values are averaged over all training set sizes, and $\hat{K}_{\mathcal{F}}$ over all class pairings (Sec. 3.2); error bars indicate 95% confidence intervals.

Models and training. We evaluate six models total: ResNet-18, -34 and -50 (He et al., 2016), and VGG-13, -16 and -19 (Simonyan & Zisserman, 2015). Each model f is trained on each dataset for its respective binary classification task with Adam (Kingma & Ba, 2015) until the model fully fits to the training set, for each training set size N described previously. We provide all training and implementation details in Appendix F, and our code can be found at https://github.com/mazurowski-lab/intrinsic-properties.

5 THE RELATIONSHIP OF GENERALIZATION WITH DATASET INTRINSIC DIMENSION AND LABEL SHARPNESS

In Fig. 1 we show the average measured intrinsic dimension $d_{\rm data}$ and label sharpness $\hat{K}_{\mathcal{F}}$ of each dataset we study. While both natural and medical datasets can range in $d_{\rm data}$, we note that medical datasets typically have much higher $\hat{K}_{\mathcal{F}}$ than natural image datasets, which we will propose may explain differences in generalization ability scaling rates between the two imaging domains. We emphasize that $d_{\rm data}$ and $K_{\mathcal{F}}$ are model-independent properties of a dataset itself. We will now describe how network generalization ability scales with $d_{\rm data}$ and $K_{\mathcal{F}}$.

5.1 BOUNDING GENERALIZATION ABILITY WITH DATASET INTRINSIC DIMENSION

A result which we will use throughout is that on average, given some N datapoints sampled i.i.d. from a d-dimensional manifold, the distance between the nearest neighbor \hat{x} of some datapoint x scales as $\mathbb{E}_x ||x - \hat{x}|| = \mathcal{O}(N^{-1/d_{\text{data}}})$ (Levina & Bickel, 2004). As such, the nearest-neighbor distance of some test point to the training set decreases as the training set grows larger by $\mathcal{O}(N^{-1/d_{\text{data}}})$. It can then be shown that the loss on the test set/generalization error scales as $\mathcal{O}(K_L \max(K_f, K_{\mathcal{F}})N^{-1/d_{\text{data}}})$ on average; this is summarized in the following theorem.

Theorem 1 (Generalization Error and Dataset Intrinsic Dim. Scaling Law (Bahri et al., 2021)). Let L, f and \mathcal{F} be Lipschitz on $\mathcal{M}_{d_{\text{data}}}$ with respective constants K_L , K_f and $K_{\mathcal{F}}$. Further let $\mathcal{D}_{\text{train}}$ be a training set of size N sampled i.i.d. from $\mathcal{M}_{d_{\text{data}}}$, with $f(x) = \mathcal{F}(x)$ for all $x \in \mathcal{D}_{\text{train}}$. Then, $L = \mathcal{O}(K_L \max(K_f, K_{\mathcal{F}})N^{-1/d_{\text{data}}})$.

 $^{^4}N=1750$ is the upper limit of N that all datasets could satisfy, given the smaller size of medical image datasets and ImageNet's typical example count per class. In Appendix C.4 we evaluate much higher N for datasets that allow for it.

We note that the $K_{\mathcal{F}}$ term is typically treated as an unknown constant in the literature (Bahri et al., 2021); instead, we propose to *estimate* it with the empirical label sharpness $\hat{K}_{\mathcal{F}}$ (Sec. 3.2). We will next show that $K_f \simeq K_{\mathcal{F}}$ for large N (common for deep models), which allows us to approximate Theorem 1 as $L \simeq \mathcal{O}(K_L K_{\mathcal{F}} N^{-1/d_{\text{data}}})$, a scaling law independent of the trained model f. Intuitively, this means that the Lipschitz smoothness of f molds to the smoothness of the label distribution as the training set grows larger and test points typically become closer to training points.

Theorem 2 (Approximating K_f with K_F). K_f converges to K_F in probability as $N \to \infty$.

We show the full proof in Appendix A.2 due to space constraints. This result is also desirable because computing an estimate for K_f , the Lipschitz constant of the model f, either using Eq. (1) or with other techniques (Fazlyab et al., 2019), depends on the choice of model f, and may require many forward passes. Estimating $K_{\mathcal{F}}$ (Eq. (1) is far more tractable, as it is an intrinsic property of the dataset itself which is relatively fast to compute.

Next, note that the Lipschitz constant K_L is a property of the loss function, which we take as fixed *a priori*, and so does not vary between datasets or models. As such, K_L can be factored out of the scaling law of interest, such that we can simply consider $L \simeq \mathcal{O}(K_{\mathcal{F}}N^{-1/d_{\text{data}}})$, *i.e.*,

$$\log L \lesssim -\frac{1}{d_{\text{data}}} \log N + \log K_{\mathcal{F}} + a \tag{2}$$

for some constant a. In the following section, we will demonstrate how the prediction of Eq. (2) may explain recent empirical results in the literature where the rate of this generalization scaling law differed drastically between natural and medical datasets, via the measured differences in the typical label sharpness $\hat{K}_{\mathcal{F}}$ of datasets in these two domains.

5.2 GENERALIZATION DISCREPANCIES BETWEEN IMAGING DOMAINS

Consider the result from Eq. (2) that the test loss/generalization error scales approximately as $L \propto K_{\mathcal{F}} N^{-1/d_{\mathrm{data}}}$ on average. From this, we hypothesize that a higher label sharpness $K_{\mathcal{F}}$ will result in the test loss curve that grows faster with respect to d_{data} .

In Fig. 2 we evaluate the generalization error (log test loss) scaling of all models trained on each natural and medical image dataset with respect to the training set intrinsic dimension $d_{\rm data}$, for all evaluated training set sizes N. We also show the scaling of test *accuracy* in Appendix E.1.

We see that within an imaging domain (natural or medical), model generalization error typically increases with $d_{\rm data}$, as predicted, similar to prior results (Pope et al., 2020; Konz et al., 2022); in particular, approximately $\log L \propto -1/d_{\rm data} + {\rm const.}$, aligning with Eq. (2). However, we also see that the generalization error scaling is much sharper for models trained on medical data than natural data; models trained on datasets with similar $d_{\rm data}$ and of the same size N tend to perform much worse if the data is medical images. A similarly large gap appears for the scaling of test accuracy (Appendix E.1). We posit that this difference is explained by medical datasets typically having much higher label sharpness ($\hat{K}_{\mathcal{F}} \sim 2.5 \times 10^{-4}$) than natural images ($\hat{K}_{\mathcal{F}} \sim 1 \times 10^{-4}$) (Fig. 1), as $K_{\mathcal{F}}$ is the only term in Eq. (2) that differs between two models with the same training set intrinsic dimension $d_{\rm data}$ and size N. Moreover, in Appendix C.1 we show that accounting for $K_{\mathcal{F}}$ increases the likelihood of the posited scaling law given the observed data. However, we note that there could certainly be other factors causing the discrepancy which are not accounted for.

Intuitively, the difference in dataset label sharpness $K_{\mathcal{F}}$ between these imaging domains is reasonable, as $K_{\mathcal{F}}$ describes how similar a dataset's images can be while still having different labels (Sec. 3.2). For natural image classification, images from different classes are typically quite visually distinct. However, in many medical imaging tasks, a change in class can be due to a small change or abnormality in the image, resulting in a higher dataset $K_{\mathcal{F}}$; for example, the presence of a small breast tumor will change the label of a breast MRI from healthy to cancer.

6 ADVERSARIAL ROBUSTNESS AND TRAINING SET LABEL SHARPNESS

In this section we present another advantage of obtaining the sharpness of the dataset label distribution (K_F) : it is negatively correlated with the adversarial robustness of a neural network. Given

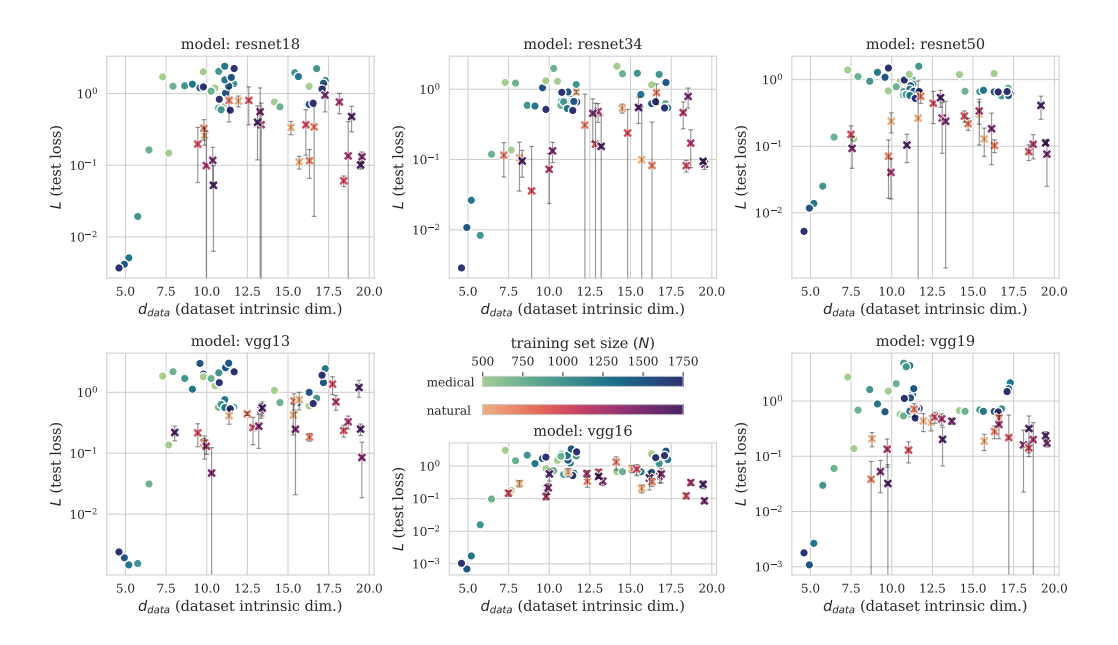


Figure 2: Scaling of log test set loss/generalization ability with training dataset intrinsic dimension $(d_{\rm data})$ for natural and medical datasets. Each point corresponds to a (model, dataset, training set size) triplet. Medical dataset results are shown in blue shades, and natural dataset results are shown in red; note the difference in generalization error scaling rate between the two imaging domains. Standard deviation error bars are shown for natural image datasets for 5 different class pairs.

some test point $x_0 \in \mathcal{M}_{d_{\text{data}}}$ with true label $y = \mathcal{F}(x_0)$, the general goal of an adversarial attack is to find some \tilde{x} that appears similar to $x_0 - i.e.$, $||\tilde{x} - x_0||_{\infty}$ is small — that results in a different, seemingly erroneous network prediction for \tilde{x} . Formally, the *robustness radius* of the trained network f at x_0 is defined by

$$R(f, x_0) := \inf_{\tilde{x}} \{ ||\tilde{x} - x_0||_{\infty} : f(\tilde{x}) \neq y \},$$
(3)

where $x_0 \in \mathcal{M}_{d_{\text{data}}}$ (Zhang et al., 2021). This describes the largest region around x_0 where f is robust to adversarial attacks. We define the *expected robust radius* of f as $\hat{R}(f) := \mathbb{E}_{x_0 \sim \mathcal{M}_{d_{\text{data}}}} R(f, x_0)$.

Theorem 3 (Adversarial Robustness and Label Sharpness Scaling Law). Let f be K_f -Lipschitz on \mathbb{R}^n . For a sufficiently large training set, the lower bound for the expected robustness radius of f scales as $\hat{R}(f) \simeq \Omega(1/K_F)$.

Proof. This follows from Prop. 1 of Tsuzuku et al. (2018) — see Appendix A.4 for all details. \Box

While it is very difficult to estimate robustness radii of neural networks in practice (Katz et al., 2017), we can instead measure the average loss penalty of f due to attack, $\mathbb{E}_{x_0 \sim \mathcal{D}_{test}}(L(\tilde{x}) - L(x_0))$, over a test set \mathcal{D}_{test} of points sampled from $\mathcal{M}_{d_{data}}$, and see if it correlates negatively with $\hat{K}_{\mathcal{F}}$ (Eq. (1)) for different models and datasets. As the expected robustness radius decreases, so should the loss penalty become steeper. We use FGSM (Goodfellow et al., 2015) attacks with L_{∞} budgets of $\epsilon \in \{1/255, 2/255, 4/225, 8/255\}$ to obtain \tilde{x} .

In Fig. 3 we plot the test loss penalty with respect to $\hat{K}_{\mathcal{F}}$ for all models and training set sizes for $\epsilon=2/255$, and show the Pearson correlation r between these quantities for each model, for all ϵ , in Table 1 (per-domain correlations are provided in Appendix E.3). (We provide the plots for the other ϵ values, as well as for the test *accuracy* penalty, in Appendix E.3). Here we average results over the different training set sizes N due to the lack of dependence of Theorem 3 on N.

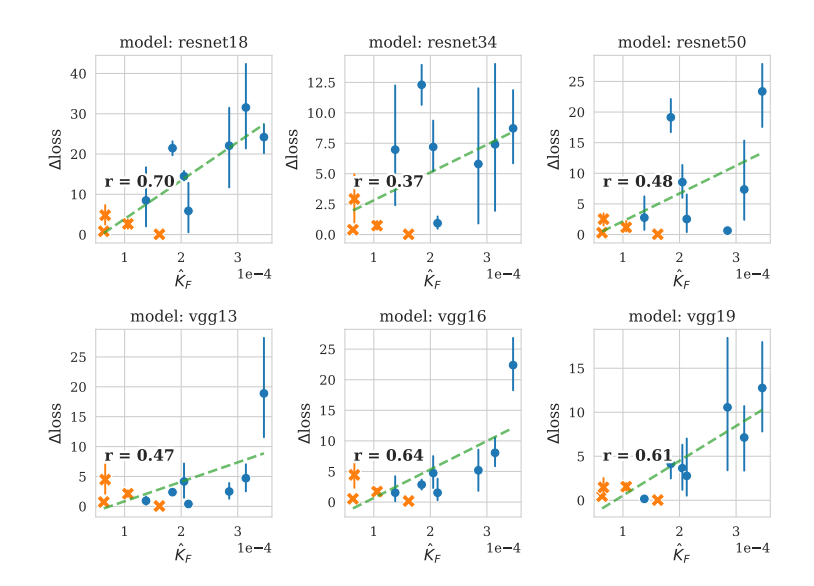


Figure 3: Test set loss penalty due to FGSM adversarial attack vs. measured dataset label sharpness $(\hat{K}_{\mathcal{F}})$ for models trained on natural and medical image datasets (orange and blue points, respectively). Pearson correlation coefficient r also shown. Error bars are 95% confidence intervals over all training set sizes N for the same dataset.

As expected, the loss penalty is typically worse for models trained on datasets with higher $K_{\mathcal{F}}$, implying a smaller expected robustness radius. We see that medical datasets, which typically have higher $K_{\mathcal{F}}$ than natural datasets (Fig. 1), are indeed typically more susceptible to attack, as was found in Ma et al. (2021). In Appendix D.1 we show example clean

Atk. ϵ		RN-34		V-13	V-16	V-19
1/255	0.77	0.48	0.55	0.47	0.63	0.61
2/255	0.70	0.37	0.48	0.47	0.64	0.61
4/255	0.63	0.26	0.41	0.45	0.62	0.6
8/255	0.54	0.18	0.34	0.39	0.58	0.57

Table 1: Pearson correlation r between test loss penalty due to FGSM attack and dataset label sharpness $\hat{K}_{\mathcal{F}}$, over all datasets and all training sizes. "RN" = ResNet, "V" = VGG.

and attacked images for each medical image dataset for $\epsilon=2/255$. A clinical practitioner may not notice any difference between the clean and attacked images upon first look,⁵ yet the attack makes model predictions completely unreliable. This indicates that adversarially-robust models may be needed for medical image analysis scenarios where potential attacks may be a concern.

7 CONNECTING REPRESENTATION INTRINSIC DIMENSION TO DATASET INTRINSIC DIMENSION AND GENERALIZATION

The scaling of network generalization ability with dataset intrinsic dimension $d_{\rm data}$ (Sec. 5.1) motivates us to study the same behavior in the space of the network's learned hidden representations for the dataset. In particular, we follow (Ansuini et al., 2019; Gong et al., 2019) and assume that an encoder in a neural network maps input images to some $d_{\rm repr}$ -dimensional manifold of *representations* (for a given layer), with $d_{\rm repr} \ll n$. As in the empirical work of Ansuini et al. (2019), we consider the intrinsic dimensionality of the representations of the final hidden layer of f. Recall that the test loss can be bounded above as $L = \mathcal{O}(K_L \max(K_f, K_{\mathcal{F}})N^{-1/d_{\rm data}})$ (Thm. 1). A similar analysis can be used to derive a loss scaling law for $d_{\rm repr}$, as follows.

Theorem 4 (Generalization Error and Learned Representation Intrinsic Dimension Scaling Law). $L \simeq \mathcal{O}(K_L N^{-1/d_{\text{repr}}})$, where K_L is the Lipschitz constant for L.

⁵That being said, the precise physical interpretation of intensity values in certain medical imaging modalities, such as Hounsfield units for CT, may reveal the attack upon close inspection.

We reserve the proof for Appendix A.3 due to length constraints, but the key is to split f into a composition of an encoder and a final layer and analyze the test loss in terms of the encoder's outputted representations. Similarly to Eq. (2), K_L is fixed for all experiments, such that we can simplify this result to $L \simeq \mathcal{O}(N^{-1/d_{\text{repr}}})$, i.e.,

$$\log L \lesssim -\frac{1}{d_{\text{repr}}} \log N + b \tag{4}$$

for some constant b. This equation is of the same form as the loss scaling law based on the *dataset* intrinsic dimension $d_{\rm data}$ of Thm. 1. This helps provide theoretical justification for prior empirical results of L increasing with $d_{\rm repr}$ (Ansuini et al. (2019), as well as for it being similar in form to the scaling of L with $d_{\rm data}$ (Fig. (2)).

In Fig. 4 we evaluate the scaling of log test loss with the $d_{\rm repr}$ of the training set (Eq. (4)), for each model, dataset, and training set size as in Sec. 5.1. The estimates of $d_{\rm repr}$ are made using TwoNN on the final hidden layer representations computed from the training set for the given model, as in Ansuini et al. (2019). We also show the scaling of test accuracy in Appendix E.1, as well as results from using the MLE estimator to compute $d_{\rm repr}$.

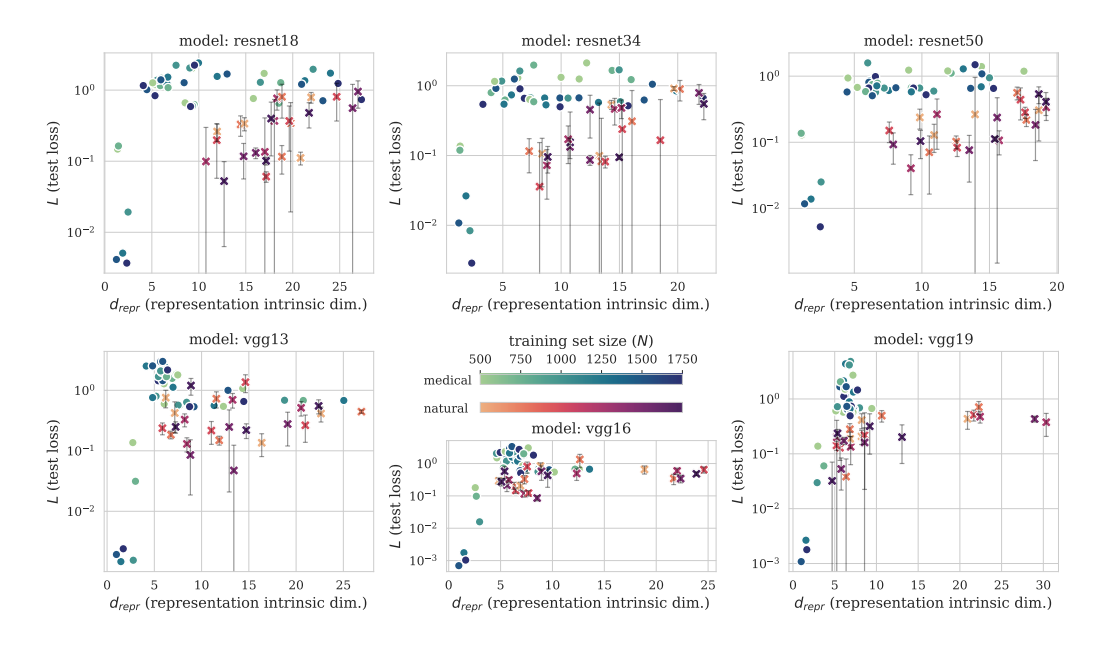


Figure 4: Scaling of log test set loss/generalization ability with the intrinsic dimension of final hidden layer learned representations of the training set (d_{repr}), for natural and medical datasets. Each point corresponds to a (model, dataset, training set size) triplet. Medical dataset results are shown in blue shades, and natural dataset results are shown in red.

We see that generalization error typically increases with $d_{\rm repr}$, in a similar shape as the $d_{\rm data}$ scaling (Fig. 2). The similarity of these curves may be explained by $d_{\rm repr} \lesssim d_{\rm data}$, or other potential factors unaccounted for. The former arises if the loss bounds of Theorems 1 and 4 are taken as *estimates*:

Theorem 5 (Bounding of Representation Intrinsic Dim. with Dataset Intrinsic Dim.). Let Theorems 1 and 4 be taken as estimates, i.e., $L \approx K_L \max(K_f, K_F) N^{-1/d_{\text{data}}}$ and $L \approx K_L N^{-1/d_{\text{repr}}}$. Then, $d_{\text{repr}} \lesssim d_{\text{data}}$.

Proof. This centers on equating the two scaling laws and using a property of the Lipschitz constant of classification networks—see Appendix A.5 for the full proof. \Box

In other words, the intrinsic dimension of the training dataset serves as an upper bound for the intrinsic dimension of the final hidden layer's learned representations. While a rough estimate, we found this to usually be the case in practice, shown in Fig. 5 for all models, datasets and training

sizes. Here, $d_{\text{repr}} = d_{\text{data}}$ is shown as a dashed line, and we use the same estimator (MLE, Sec. 3.1) for d_{data} and d_{repr} for consistency (similar results using TwoNN are shown in Appendix E.2).

Intuitively, we would expect d_{repr} to be bounded by d_{data} , as d_{data} encapsulates all raw dataset information, while learned representations prioritize task-related information and discard irrelevant details (Tishby & Zaslavsky, 2015), resulting in $d_{\text{repr}} \lesssim d_{\text{data}}$. Future work could investigate how this relationship varies for networks trained on different tasks, including supervised (e.g., segmentation, detection) and self-supervised or unsupervised learning, where d_{repr} might approach d_{data} .

DISCUSSION AND CONCLUSIONS

In this paper, we explored how the generalization ability and adversarial robustness of a neural network relate to the intrinsic properties of its training set, such as intrinsic dimension $(d_{\rm data})$ and label sharpness $(K_{\mathcal{F}})$. We chose radiological and natural image domains as prominent examples, but our approach was quite general; indeed, in Appendix C.2 we evaluate our hypotheses on a skin lesion image dataset, a domain that shares similarities with both natural images and radiological images, and intriguingly find that properties of the dataset and models trained on it often lie in between these two domains. It would be interesting to study these relationships in still other imaging domains such as satellite imaging (Pritt & Chern, 2017), histopathology (Komura & Ishikawa, 2018), and others. Additionally, this analysis could be extended to other tasks (e.g., multi-class classification or semantic segmentation), newer model architectures such as ConvNeXt (Liu et al., 2022), non-convolutional models such as MLPs or vision transformers (Dosovitskiy et al., 2021), or even natural language models.

Our findings may provide practical uses beyond merely a better theoretical understanding of these phenomena. For example, we provide a short example of using the network generalization dependence on label sharpness to rank the predicted learning difficulty of different tasks for the same dataset in Appendix C.3. Additionally, the minimum number of annotations needed for an unlabeled training set of images could be inferred given the measured d_{data} of the dataset and some desired test loss (Eq. (2)), which depends on the imaging domain of the dataset (Fig. 2).⁶ This is especially relevant to medical images, where creating quality annotations can be expensive and time-consuming. Additionally, Sec. 6 demonstrates the importance of using adversarially robust models or training techniques for more vulnerable domains. Finally, the relation of learned representation intrinsic dimension to generalization ability (Sec. 7) and dataset intrinsic dimension (Theorem 5) could inform the minimum parameter count of network bottleneck layers.

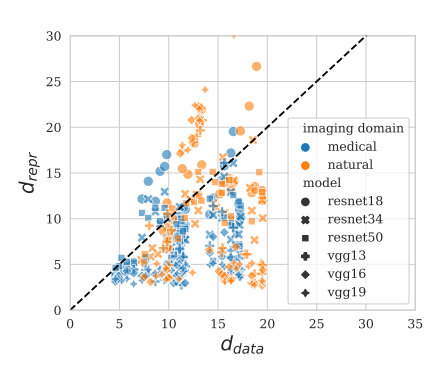


Figure 5: Training set intrinsic dimension upper-bounds learned representation intrinsic dimension. Each point corresponds to a (model, dataset, training set size) triplet.

A limitation of our study is that despite our best efforts, it is difficult to definitively say if training set label sharpness $(K_{\mathcal{F}})$ causes the observed generalization scaling discrepancy between natural and medical image models (Sec. 5.1, Fig. 2). We attempted to rule out alternatives via our formal analysis and by constraining many factors in our experiments (e.g., model, loss, training and test set sizes, data sampling strategy, etc.). Additionally, we found that accounting for $K_{\mathcal{F}}$ in the generalization scaling law increases the likelihood of the law given our observed data (Appendix C.1). Altogether, our results tell us that $K_{\mathcal{F}}$ constitutes an important difference between natural and medical image datasets, but other potential factors unaccounted for should still be considered.

Our findings provide insights into how neural network behavior varies within and between the two crucial domains of natural and medical images, enhancing our understanding of generalization, representation learning, and robustness.

⁶Note that doing so in practice by fitting the scaling law model to existing (L, N, d_{data}) results would require first evaluating a wider range of N due to the logarithmic dependence of Eq. (2) on N.

AUTHOR CONTRIBUTIONS

N.K. wrote the paper, derived the mathematical results, ran the experiments, and created the visualizations. M.A.M. helped revise the paper, the presentation of the results, and the key takeaways.

ACKNOWLEDGMENTS

The authors would like to thank Hanxue Gu and Haoyu Dong for helpful discussion and inspiration.

References

- Rayna Andreeva, Katharina Limbeck, Bastian Rieck, and Rik Sarkar. Metric space magnitude and generalisation in neural networks. *arXiv preprint arXiv:2305.05611*, 2023.
- Alessio Ansuini, Alessandro Laio, Jakob H Macke, and Davide Zoccolan. Intrinsic dimension of data representations in deep neural networks. *Advances in Neural Information Processing Systems*, 32, 2019.
- Yasaman Bahri, Ethan Dyer, Jared Kaplan, Jaehoon Lee, and Utkarsh Sharma. Explaining neural scaling laws. *arXiv preprint arXiv:2102.06701*, 2021.
- Louis Béthune, Thibaut Boissin, Mathieu Serrurier, Franck Mamalet, Corentin Friedrich, and Alberto Gonzalez Sanz. Pay attention to your loss: understanding misconceptions about lipschitz neural networks. *Advances in Neural Information Processing Systems*, 35:20077–20091, 2022.
- Tolga Birdal, Aaron Lou, Leonidas J Guibas, and Umut Simsekli. Intrinsic dimension, persistent homology and generalization in neural networks. Advances in Neural Information Processing Systems, 34:6776–6789, 2021.
- Bradley CA Brown, Anthony L. Caterini, Brendan Leigh Ross, Jesse C Cresswell, and Gabriel Loaiza-Ganem. Verifying the union of manifolds hypothesis for image data. In *The Eleventh International Conference on Learning Representations*, 2023. URL https://openreview.net/forum?id=Rvee9CAX4fi.
- Ethan Caballero, Kshitij Gupta, Irina Rish, and David Krueger. Broken neural scaling laws. In *The Eleventh International Conference on Learning Representations*, 2023. URL https://openreview.net/forum?id=sckjveqlCZ.
- Noel CF Codella, David Gutman, M Emre Celebi, Brian Helba, Michael A Marchetti, Stephen W Dusza, Aadi Kalloo, Konstantinos Liopyris, Nabin Mishra, Harald Kittler, et al. Skin lesion analysis toward melanoma detection: A challenge at the 2017 international symposium on biomedical imaging (isbi), hosted by the international skin imaging collaboration (isic). In 2018 IEEE 15th international symposium on biomedical imaging (ISBI 2018), pp. 168–172. IEEE, 2018.
- Jia Deng, Wei Dong, Richard Socher, Li-Jia Li, Kai Li, and Li Fei-Fei. Imagenet: A large-scale hierarchical image database. In *2009 IEEE conference on computer vision and pattern recognition*, pp. 248–255. Ieee, 2009.
- Li Deng. The mnist database of handwritten digit images for machine learning research [best of the web]. *IEEE signal processing magazine*, 29(6):141–142, 2012.
- Alexey Dosovitskiy, Lucas Beyer, Alexander Kolesnikov, Dirk Weissenborn, Xiaohua Zhai, Thomas Unterthiner, Mostafa Dehghani, Matthias Minderer, Georg Heigold, Sylvain Gelly, Jakob Uszkoreit, and Neil Houlsby. An image is worth 16x16 words: Transformers for image recognition at scale. In *International Conference on Learning Representations*, 2021. URL https://openreview.net/forum?id=YicbFdNTTy.
- Elena Facco, Maria d'Errico, Alex Rodriguez, and Alessandro Laio. Estimating the intrinsic dimension of datasets by a minimal neighborhood information. *Scientific reports*, 7(1):12140, 2017.
- Mahyar Fazlyab, Alexander Robey, Hamed Hassani, Manfred Morari, and George Pappas. Efficient and accurate estimation of lipschitz constants for deep neural networks. *Advances in Neural Information Processing Systems*, 32, 2019.

- Charles Fefferman, Sanjoy Mitter, and Hariharan Narayanan. Testing the manifold hypothesis. *Journal of the American Mathematical Society*, 29(4):983–1049, 2016.
- Adam E Flanders, Luciano M Prevedello, George Shih, Safwan S Halabi, Jayashree Kalpathy-Cramer, Robyn Ball, John T Mongan, Anouk Stein, Felipe C Kitamura, Matthew P Lungren, et al. Construction of a machine learning dataset through collaboration: the rsna 2019 brain ct hemorrhage challenge. *Radiology: Artificial Intelligence*, 2(3):e190211, 2020.
- Bolin Gao and Lacra Pavel. On the properties of the softmax function with application in game theory and reinforcement learning. *arXiv* preprint arXiv:1704.00805, 2017.
- Sixue Gong, Vishnu Naresh Boddeti, and Anil K Jain. On the intrinsic dimensionality of image representations. In *Proceedings of the IEEE/CVF Conference on Computer Vision and Pattern Recognition*, pp. 3987–3996, 2019.
- Ian J. Goodfellow, Jonathon Shlens, and Christian Szegedy. Explaining and harnessing adversarial examples. In Yoshua Bengio and Yann LeCun (eds.), 3rd International Conference on Learning Representations, ICLR 2015, San Diego, CA, USA, May 7-9, 2015, Conference Track Proceedings, 2015. URL http://arxiv.org/abs/1412.6572.
- Kaiming He, Xiangyu Zhang, Shaoqing Ren, and Jian Sun. Deep residual learning for image recognition. In *Proceedings of the IEEE conference on computer vision and pattern recognition*, pp. 770–778, 2016.
- Jordan Hoffmann, Sebastian Borgeaud, Arthur Mensch, Elena Buchatskaya, Trevor Cai, Eliza Rutherford, Diego de Las Casas, Lisa Anne Hendricks, Johannes Welbl, Aidan Clark, et al. Training compute-optimal large language models. *arXiv preprint arXiv:2203.15556*, 2022.
- Jeremy Irvin, Pranav Rajpurkar, Michael Ko, Yifan Yu, Silviana Ciurea-Ilcus, Chris Chute, Henrik Marklund, Behzad Haghgoo, Robyn Ball, Katie Shpanskaya, et al. Chexpert: A large chest radiograph dataset with uncertainty labels and expert comparison. In *Proceedings of the AAAI conference on artificial intelligence*, volume 33, pp. 590–597, 2019.
- Jared Kaplan, Sam McCandlish, Tom Henighan, Tom B Brown, Benjamin Chess, Rewon Child, Scott Gray, Alec Radford, Jeffrey Wu, and Dario Amodei. Scaling laws for neural language models. arXiv preprint arXiv:2001.08361, 2020.
- Guy Katz, Clark Barrett, David L Dill, Kyle Julian, and Mykel J Kochenderfer. Reluplex: An efficient smt solver for verifying deep neural networks. In *Computer Aided Verification: 29th International Conference, CAV 2017, Heidelberg, Germany, July 24-28, 2017, Proceedings, Part I 30*, pp. 97–117. Springer, 2017.
- Diederik P. Kingma and Jimmy Ba. Adam: A method for stochastic optimization. In Yoshua Bengio and Yann LeCun (eds.), 3rd International Conference on Learning Representations, ICLR 2015, San Diego, CA, USA, May 7-9, 2015, Conference Track Proceedings, 2015. URL http://arxiv.org/abs/1412.6980.
- Daisuke Komura and Shumpei Ishikawa. Machine learning methods for histopathological image analysis. *Computational and structural biotechnology journal*, 16:34–42, 2018.
- Nicholas Konz, Hanxue Gu, Haoyu Dong, and Maciej A Mazurowski. The intrinsic manifolds of radiological images and their role in deep learning. In *Medical Image Computing and Computer Assisted Intervention–MICCAI 2022: 25th International Conference, Singapore, September 18–22, 2022, Proceedings, Part VIII*, pp. 684–694. Springer, 2022.
- Alex Krizhevsky, Geoffrey Hinton, et al. Learning multiple layers of features from tiny images. 2009.
- Henry Kvinge, Davis Brown, and Charles Godfrey. Exploring the representation manifolds of stable diffusion through the lens of intrinsic dimension. *ICLR 2023 Workshop on Mathematical and Empirical Understanding of Foundation Models*, 2023.
- Elizaveta Levina and Peter Bickel. Maximum likelihood estimation of intrinsic dimension. *Advances in neural information processing systems*, 17, 2004.

- Zhuang Liu, Hanzi Mao, Chao-Yuan Wu, Christoph Feichtenhofer, Trevor Darrell, and Saining Xie. A convnet for the 2020s. In *Proceedings of the IEEE/CVF conference on computer vision and pattern recognition*, pp. 11976–11986, 2022.
- Xingjun Ma, Yuhao Niu, Lin Gu, Yisen Wang, Yitian Zhao, James Bailey, and Feng Lu. Understanding adversarial attacks on deep learning based medical image analysis systems. *Pattern Recognition*, 110:107332, 2021.
- David JC MacKay and Zoubin Ghahramani. Comments on'maximum likelihood estimation of intrinsic dimension'by e. levina and p. bickel (2004). *The Inference Group Website, Cavendish Laboratory, Cambridge University*, 2005.
- Bjoern H Menze, Andras Jakab, Stefan Bauer, Jayashree Kalpathy-Cramer, Keyvan Farahani, Justin Kirby, Yuliya Burren, Nicole Porz, Johannes Slotboom, Roland Wiest, et al. The multimodal brain tumor image segmentation benchmark (brats). *IEEE transactions on medical imaging*, 34 (10):1993–2024, 2014.
- Yuval Netzer, Tao Wang, Adam Coates, Alessandro Bissacco, Bo Wu, and Andrew Y Ng. Reading digits in natural images with unsupervised feature learning. 2011.
- Phil Pope, Chen Zhu, Ahmed Abdelkader, Micah Goldblum, and Tom Goldstein. The intrinsic dimension of images and its impact on learning. In *International Conference on Learning Representations*, 2020.
- Mark Pritt and Gary Chern. Satellite image classification with deep learning. In 2017 IEEE applied imagery pattern recognition workshop (AIPR), pp. 1–7. IEEE, 2017.
- Pranav Rajpurkar, Jeremy Irvin, Aarti Bagul, Daisy Ding, Tony Duan, Hershel Mehta, Brandon Yang, Kaylie Zhu, Dillon Laird, Robyn L Ball, et al. Mura: Large dataset for abnormality detection in musculoskeletal radiographs. *arXiv* preprint arXiv:1712.06957, 2017.
- Ashirbani Saha, Michael R Harowicz, Lars J Grimm, Connie E Kim, Sujata V Ghate, Ruth Walsh, and Maciej A Mazurowski. A machine learning approach to radiogenomics of breast cancer: a study of 922 subjects and 529 dce-mri features. *British journal of cancer*, 119(4):508–516, 2018.
- Karen Simonyan and Andrew Zisserman. Very deep convolutional networks for large-scale image recognition. In Yoshua Bengio and Yann LeCun (eds.), 3rd International Conference on Learning Representations, ICLR 2015, San Diego, CA, USA, May 7-9, 2015, Conference Track Proceedings, 2015. URL http://arxiv.org/abs/1409.1556.
- Geoffrey A Sonn, Shyam Natarajan, Daniel JA Margolis, Malu MacAiran, Patricia Lieu, Jiaoti Huang, Frederick J Dorey, and Leonard S Marks. Targeted biopsy in the detection of prostate cancer using an office based magnetic resonance ultrasound fusion device. *The Journal of urology*, 189(1):86–92, 2013.
- Naftali Tishby and Noga Zaslavsky. Deep learning and the information bottleneck principle. In 2015 ieee information theory workshop (itw), pp. 1–5. IEEE, 2015.
- Aleksei Tiulpin, Jérôme Thevenot, Esa Rahtu, Petri Lehenkari, and Simo Saarakkala. Automatic Knee Osteoarthritis Diagnosis from Plain Radiographs: A Deep Learning-Based Approach. *Scientific Reports*, 8(1):1727, 2018. ISSN 2045-2322. doi: 10.1038/s41598-018-20132-7. URL https://doi.org/10.1038/s41598-018-20132-7.
- Hugo Touvron, Louis Martin, Kevin Stone, Peter Albert, Amjad Almahairi, Yasmine Babaei, Nikolay Bashlykov, Soumya Batra, Prajjwal Bhargava, Shruti Bhosale, et al. Llama 2: Open foundation and fine-tuned chat models. *arXiv preprint arXiv:2307.09288*, 2023.
- Yusuke Tsuzuku, Issei Sato, and Masashi Sugiyama. Lipschitz-margin training: Scalable certification of perturbation invariance for deep neural networks. *Advances in neural information processing systems*, 31, 2018.

- Pauli Virtanen, Ralf Gommers, Travis E. Oliphant, Matt Haberland, Tyler Reddy, David Cournapeau, Evgeni Burovski, Pearu Peterson, Warren Weckesser, Jonathan Bright, Stéfan J. van der Walt, Matthew Brett, Joshua Wilson, K. Jarrod Millman, Nikolay Mayorov, Andrew R. J. Nelson, Eric Jones, Robert Kern, Eric Larson, C J Carey, İlhan Polat, Yu Feng, Eric W. Moore, Jake VanderPlas, Denis Laxalde, Josef Perktold, Robert Cimrman, Ian Henriksen, E. A. Quintero, Charles R. Harris, Anne M. Archibald, Antônio H. Ribeiro, Fabian Pedregosa, Paul van Mulbregt, and SciPy 1.0 Contributors. SciPy 1.0: Fundamental Algorithms for Scientific Computing in Python. Nature Methods, 17:261–272, 2020. doi: 10.1038/s41592-019-0686-2.
- Quang H Vuong. Likelihood ratio tests for model selection and non-nested hypotheses. *Econometrica: journal of the Econometric Society*, pp. 307–333, 1989.
- Jiancheng Yang, Rui Shi, Donglai Wei, Zequan Liu, Lin Zhao, Bilian Ke, Hanspeter Pfister, and Bingbing Ni. Medmnist v2-a large-scale lightweight benchmark for 2d and 3d biomedical image classification. *Scientific Data*, 10(1):41, 2023.
- Bohang Zhang, Tianle Cai, Zhou Lu, Di He, and Liwei Wang. Towards certifying l-infinity robustness using neural networks with l-inf-dist neurons. In *International Conference on Machine Learning*, pp. 12368–12379. PMLR, 2021.

Part I

Supplementary Materials

Table of Contents

A	Mathematical Details and Proofs	14
	A.1 Extension of Results to Multi-Class Classification	14
	A.2 Proof of Theorem 2 (Approximating K_f with K_F)	15
	A.3 Proof of Theorem 4 (Generalization Error and Representation Intrinsic Dim. Scal-	
	ing Law)	15
	8,	16
	A.5 Proof of Theorem 5 (Bounding of Representation Intrinsic Dim. with Dataset	
	Intrinsic Dim.)	16
В	Analysis of Intrinsic Dataset Property Characteristics (Intrinsic Dimension and La-	
	F	17
	3.1 Invariance of Intrinsic Dataset Properties to Transformations	17
\mathbf{C}	Additional Results, Extensions, and Applications	18
	C.1 Likelihood Analysis of Theoretical and Empirical Generalization Scaling Laws . 1	18
	C.2 Evaluating a Dataset from an Additional Domain	19
	C.3 Practical Application: Task Selection for Medical Images	20
	C.4 Evaluation at Much Higher Training Set Sizes	21
	C.5 Dependence of Network Performance on Image Resolution	22
D	Additional Visualizations	22
	D.1 Example Adversarial Attacks on Medical Images	22
E	Main Results with Other Metrics	23
	E.1 Generalization Scaling with d_{data} and d_{repr}	23
	E.2 Bounding Hidden Representation Intrinsic Dimension with Dataset Intrinsic Di-	
		26
	E.3 Adversarial Robustness scaling with $\hat{K}_{\mathcal{F}}$	26
F	Training and Implementational Details	27
G	Medical Image Dataset Details	30

A MATHEMATICAL DETAILS AND PROOFS

A.1 EXTENSION OF RESULTS TO MULTI-CLASS CLASSIFICATION

Generalization scaling laws. Our results extend naturally from binary classification to multi-class classification. Given some test point x_0 of some unknown target class, if x'_{tr} is the nearest neighbor to x_0 in the training set of the same class (both on $\mathcal{M}_{d_{\text{data}}}$), the term $\mathbb{E}_{\mathcal{D}_{\text{train}} \sim \mathcal{M}_{d_{\text{data}}}} ||x_0 - x'_{tr}||$ scales in expectation as

$$\mathcal{O}\left(\left(\frac{N+1}{C}\right)^{-1/d_{\text{data}}}\right) \simeq \mathcal{O}\left(\left(\frac{N}{C}\right)^{-1/d_{\text{data}}}\right) = \mathcal{O}(N^{-1/d_{\text{data}}}),\tag{5}$$

where C is the total number of classes, assuming the classes to be evenly sampled in the training set. The same logic can be used for the intrinsic representation dimension d_{repr} to show $\mathcal{O}\left(\left(\frac{N+1}{C}\right)^{-1/d_{\text{repr}}}\right) \simeq \mathcal{O}(N^{-1/d_{\text{repr}}})$. Therefore, the asymptotic upper bounds in the d_{data} and d_{repr} scaling laws (Theorems 1 and 4, respectively) still hold, as well as the derived result of Theorem 5.

Label sharpness. The label sharpness metric $\hat{K}_{\mathcal{F}}$ (Eq. 1) was formulated under the binary classification scenario, where data is either labeled with 0 or 1 (Sec. 3). However, it could potentially be extended to the multi-class scenario by simply replacing the $|y_j - y_k|$ term in the numerator of Eq. 1 with the indicator function $1_{y_j \neq y_k}$ as

$$\hat{K}_{\mathcal{F}} := \max_{j,k} \left(\frac{1_{y_j \neq y_k}}{||x_j - x_k||} \right),\tag{6}$$

which clearly simplifies to Eq. 1 for binary classification. This modification prevents $\hat{K}_{\mathcal{F}}$ from being biased by the numerical value of labels given to different classes, but a more careful extension could be pursued in the future to confirm a properly theoretically-motivated multi-class label sharpness metric.

A.2 PROOF OF THEOREM 2 (APPROXIMATING K_f WITH $K_{\mathcal{F}}$)

Proof. Let x_1 and x_2 be arbitrary datapoints sampled from $\mathcal{M}_{d_{\text{data}}}$, with nearest neighbors in the training set $\mathcal{D}_{\text{train}}$ of \hat{x}_1 and \hat{x}_2 , respectively. Then,

$$|f(x_1) - f(x_2)| = |f(x_1) - f(x_2) + (\mathcal{F}(x_1) - \mathcal{F}(x_1) + \mathcal{F}(x_2) - \mathcal{F}(x_2) + f(\hat{x}_1) - f(\hat{x}_1) + f(\hat{x}_2) - f(\hat{x}_2)|$$

$$\leq |f(x_1) - f(\hat{x}_1)| + |f(x_2) - f(\hat{x}_2)| + |\mathcal{F}(x_1) - \mathcal{F}(x_2)| + |f(\hat{x}_2) - \mathcal{F}(x_2)|, \quad (7)$$

by the triangle inequality. Because we assumed that $f(x) = \mathcal{F}(x) \, \forall x \in \mathcal{D}_{\text{train}}$, i.e., the model is well-trained, the last two terms can be changed so that we have

$$|f(x_1) - f(x_2)| \le |f(x_1) - f(\hat{x}_1)| + |f(x_2) - f(\hat{x}_2)| + |\mathcal{F}(x_1) - \mathcal{F}(x_2)| + |\mathcal{F}(\hat{x}_1) - \mathcal{F}(x_1)| + |\mathcal{F}(\hat{x}_2) - \mathcal{F}(x_2)|.$$
(8)

Using the Lipschitz continuity of f and \mathcal{F} , we have that

$$|f(x_1) - f(x_2)| \le K_f(||x_1 - \hat{x}_1|| + ||x_2 - \hat{x}_2||) + K_F(||x_1 - x_2|| + ||x_1 - \hat{x}_1|| + ||x_2 - \hat{x}_2||)$$

$$= K_F||x_1 - x_2|| + (K_f + K_F)(||x_1 - \hat{x}_1|| + ||x_2 - \hat{x}_2||). \quad (9)$$

Recall that the expected nearest-neighbor distance on $\mathcal{M}_{d_{\text{data}}}$ for some N samples scales as $\mathcal{O}(N^{-1/d_{\text{data}}})$. Then, $\mathbb{E}||x_1 - \hat{x}_1|| = \mathbb{E}||x_2 - \hat{x}_2|| = \mathcal{O}((N+1)^{-1/d_{\text{data}}}) \simeq \mathcal{O}(N^{-1/d_{\text{data}}})$. If we take the expectation of both sides of Eq. (9) over the training set, we can use this fact to obtain

$$\mathbb{E}\left|f(x_1) - f(x_2)\right| \le K_{\mathcal{F}} \mathbb{E}\left|\left|x_1 - x_2\right|\right| + \mathcal{O}(\max(K_f, K_{\mathcal{F}})(N^{-1/d_{\text{data}}})). \tag{10}$$

But, the term on the right goes to zero as $N \to \infty$, so then $\Pr(|f(x_1) - f(x_2)| \le K_{\mathcal{F}}||x_1 - x_2||) \to 1$ as $N \to \infty$, or in other words, the probability that f is Lipschitz with the same constant $K_{\mathcal{F}}$ of \mathcal{F} . (A very similar proof can also be made to show that $\Pr(|\mathcal{F}(x_1) - \mathcal{F}(x_2)| \le K_f||x_1 - x_2||) \to 1$ as $N \to \infty$). Therefore, the Lipschitz constant of f converges to $K_{\mathcal{F}}$ in probability, or in other words, $K_f \to K_{\mathcal{F}}$.

A.3 PROOF OF THEOREM 4 (GENERALIZATION ERROR AND REPRESENTATION INTRINSIC DIM. SCALING LAW)

Proof. Let f be written as a composition of an encoder g, which outputs the final hidden representations of the input image, and a final output sigmoid (or softmax for multi-class classification) layer h, as $f = h \circ g$. Write the true label function $\mathcal F$ similarly, as some $\mathcal F = \mathcal H \circ \mathcal G$ for unknown $\mathcal H$ and $\mathcal G$ analogous to h and g. Assume h and $\mathcal H$ to be Lipschitz with respective constants K_h and $K_{\mathcal H}$. Analogous to assuming $f(x) = \mathcal F(x)$ for all x in the training set $\mathcal D_{\mathrm{train}}$, posit a similar claim of $g(x) = \mathcal G(x) := z$, and $h(z) = \mathcal H(z)$, $\forall x \in \mathcal D_{\mathrm{train}}$.

Let x be from the training set $\mathcal{D}_{\text{train}}$ with nearest neighbor (also in the training set) \hat{x} . Recall that we assume that $g(x) = \mathcal{G}(x) \, \forall x \in \mathcal{D}_{\text{train}}$, and that the loss vanishes at the true target label, as in Bahri et al. (2021). Let z = g(x) and $\hat{z} = g(\hat{x})$.

Then, as we assumed f and \mathcal{F} to be Lipschitz,

$$\ell(f(x)) = |\ell(f(x)) - \ell(\mathcal{F}(x))| \le K_L |f(x) - \mathcal{F}(x)| \tag{11}$$

$$= K_L|h(g(x)) - \mathcal{H}(\mathcal{G}(x))| = K_L|h(z) - \mathcal{H}(z)| \tag{12}$$

where $\ell(f(x))$ is the loss evaluated at a single datapoint, and the first equality is due to the loss vanishing at the true target label $(\ell(\mathcal{F}(x)) = 0)$, and being non-negative. Continuing,

$$\ell(f(x)) \le K_L |h(z) - \mathcal{H}(z)| \tag{13}$$

$$= K_L |h(z) - \mathcal{H}(z) + (h(\hat{z}) - h(\hat{z}) + \mathcal{H}(\hat{z}) - \mathcal{H}(\hat{z}))|$$
(14)

$$\leq K_L(|h(z) - h(\hat{z})| + |\mathcal{H}(z) - \mathcal{H}(\hat{z})| + |h(\hat{z}) - \mathcal{H}(\hat{z})|),$$
 (15)

with the last line from the triangle inequality. As $h(z) = \mathcal{H}(z)$ for all $\{z = g(x) : x \in \mathcal{D}_{\text{train}}\}$, the last term vanishes, allowing us to write

$$\ell(f(x)) \le K_L \left(|h(z) - h(\hat{z})| + |\mathcal{H}(z) - \mathcal{H}(\hat{z})| \right) \tag{16}$$

$$\leq K_L(K_h||z-\hat{z}||+K_H||z-\hat{z}||) = K_L(K_h+K_H)||z-\hat{z}||, \tag{17}$$

so then

$$\ell(f(x)) \le K_L(K_h||z - \hat{z}|| + K_H||z - \hat{z}||) = K_L(K_h + K_H)||z - \hat{z}||, \tag{18}$$

and

$$L = \underset{x \sim \mathcal{D}_{\text{test}}}{\mathbb{E}} \ell(f(x)) \le K_L(K_h + K_{\mathcal{H}}) \underset{z, \hat{z} \sim \mathcal{D}_{\text{train}}}{\mathbb{E}} ||z - \hat{z}||, \tag{19}$$

where the rightmost expectation is taken over all $\{z=g(x):x\in\mathcal{D}_{\text{train}}\}$ with corresponding nearest neighbor \hat{z} (on the representation manifold). As the expectation of the nearest-neighbor distance of the representations on the manifold scales as $\mathcal{O}(N^{-1/d_{\text{repr}}})$, it follows that

$$L = \mathcal{O}(K_L \max(K_h, K_{\mathcal{H}}) N^{-1/d_{\text{repr}}}). \tag{20}$$

Because $h=\mathcal{H}$ on the training set representations, the same procedure as the proof for Theorem 2 can be used to show that $K_{\mathcal{H}} \simeq K_h$. Finally, note that the output layer h was assumed to be a sigmoid. As the standard sigmoid (or softmax) layer is 1-Lipschitz (Gao & Pavel, 2017), $K_{\mathcal{H}} \simeq K_h = 1$, so then

$$L \simeq \mathcal{O}(K_L N^{-1/d_{\text{repr}}}). \tag{21}$$

A.4 PROOF OF THEOREM 3 (ADVERSARIAL ROBUSTNESS AND LABEL SHARPNESS SCALING LAW)

Proof. Proposition 1 of (Tsuzuku et al., 2018) states that $\hat{R}(f,x_0) \geq M_{f,x_0}/(\sqrt{2}K_f)$ where $M_{f,x_0} > 0$ is the prediction margin, the difference between the target class prediction and the highest non-target class prediction of $f(x_0)$. Applying Thm. 2 given sufficiently large N then gives $\hat{R}(f) = \mathbb{E}_{x_0 \sim \mathcal{M}_{d_{\text{data}}}} \hat{R}(f,x_0) \geq \mathbb{E}_{x_0 \sim \mathcal{M}_{d_{\text{data}}}} M_{f,x_0}/(\sqrt{2}K_f) = \Omega\left(1/K_f\right) \simeq \Omega\left(1/K_\mathcal{F}\right)$.

A.5 PROOF OF THEOREM 5 (BOUNDING OF REPRESENTATION INTRINSIC DIM. WITH DATASET INTRINSIC DIM.)

Proof. The estimation assumption implies that

$$K_L \max(K_f, K_F) N^{-1/d_{\text{data}}} \approx K_L N^{-1/d_{\text{repr}}} \quad \Rightarrow \quad N^{-1/d_{\text{data}}} \approx \frac{N^{-1/d_{\text{repr}}}}{\max(K_f, K_F)},$$
 (22)

after which taking the logarithm of both sides gives

$$\begin{cases} d_{\text{repr}} \lesssim d_{\text{data}} & \text{if } K_f, K_{\mathcal{F}} \leq 1\\ d_{\text{repr}} \gtrsim d_{\text{data}} & \text{otherwise,} \end{cases}$$
 (23)

i.e., $d_{\text{repr}} \lesssim d_{\text{data}}$ if the trained model f and target model \mathcal{F} are 1-Lipschitz (with respect to nearest neighbors in the training set).

Now, note that in our classification task setting, the decision boundaries/predictions of some K-Lipschitz network f are the same as the 1-Lipschitz version $\frac{1}{K}f$ (Béthune et al., 2022). As such, the scaling behavior we analyze here of L vs. d_{repr} is the same as if $K_f = 1$. As $K_{\mathcal{F}} \simeq K_f$ (Theorem 2), Eq. (23) can be simplified to just $d_{\text{repr}} \lesssim d_{\text{data}}$. In practice, we also found that all datasets had $K_{\mathcal{F}} \ll 1$ (Fig. 1), so the first case of Eq. (23) should hold true anyways.

B ANALYSIS OF INTRINSIC DATASET PROPERTY CHARACTERISTICS (INTRINSIC DIMENSION AND LABEL SHARPNESS)

B.1 INVARIANCE OF INTRINSIC DATASET PROPERTIES TO TRANSFORMATIONS

In Fig. 6, left, we show that measured dataset intrinsic dimension $d_{\rm data}$ estimates are barely affected by image resizing over a range of resolutions (square image sizes of [32, 64, 128, 256, 512]), with the specific example of 32×32 shown in the right of Fig. 7. We show the similar result of measured dataset label sharpness $\hat{K}_{\mathcal{F}}$ being invariant to image resizing in Fig. 6, right, and Fig. 8, right, besides all datasets' $\hat{K}_{\mathcal{F}}$ values being multiplied by the same positive constant (i.e., the relative placement of the $\hat{K}_{\mathcal{F}}$ of each dataset stays the same with respect to such transformations). Because this constant is the same for all datasets for the given image resolution, it has no effect on the scaling law result of Eq. (2), as it can be folded into the constant a.

We show similar results for modifying the channel count of images (*i.e.*, modifying all grayscale images to RGB) in the left of Figs. 7 and 8.

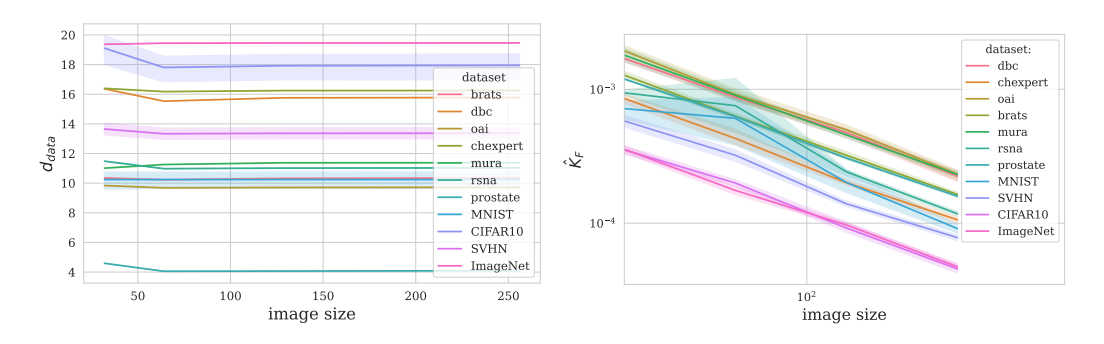


Figure 6: Left: Dependence of measured intrinsic dimension $(d_{\rm data})$ of the image datasets which we analyze with respect to image size (height and width). $d_{\rm data}$ values are averaged over all training set sizes; error bars indicate 95% confidence intervals. Right: Same, but for measured dataset label sharpness $\hat{K}_{\mathcal{F}}$. $\hat{K}_{\mathcal{F}}$ values are averaged over all class pairings (Sec. 3.2); error bars indicate 95% confidence intervals.

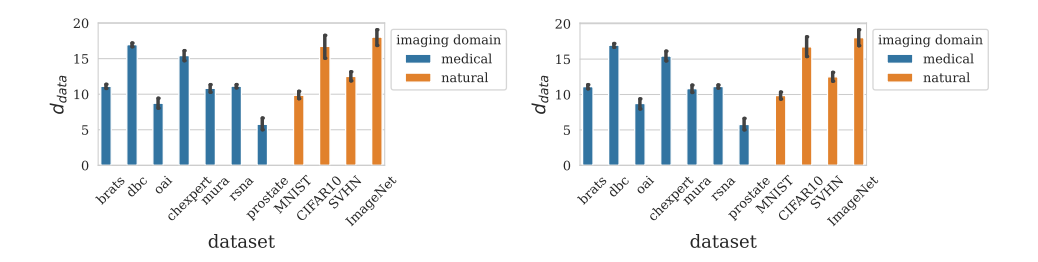


Figure 7: Measured intrinsic dimension ($d_{\rm data}$) of the natural (orange) and medical (blue) image datasets which we analyze (Sec. 4), for all images changed to RGB/3-channel (**left**), and all images resized to 32×32 (**right**). $d_{\rm data}$ values are averaged over all training set sizes; error bars indicate 95% confidence intervals. Compare to the default results in Fig. 1, left (224×224 , original image channel counts) for reference.

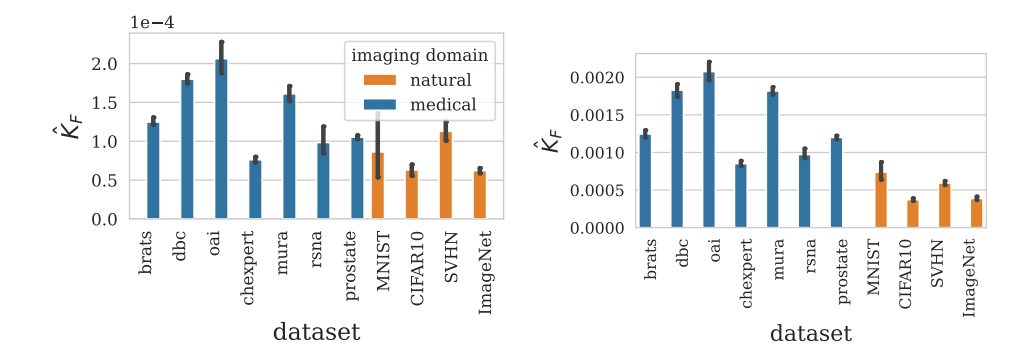


Figure 8: Measured label sharpnesses $(\hat{K}_{\mathcal{F}})$ of the natural (orange) and medical (blue) image datasets which we analyze (Sec. 4), for all images changed to RGB/3-channel (**left**), and all images resized to 32×32 (**right**). $\hat{K}_{\mathcal{F}}$ values are averaged over all class pairings (Sec. 3.2); error bars indicate 95% confidence intervals. Compare to the default results in Fig. 1, right (224×224 , original image channel counts) for reference.

C ADDITIONAL RESULTS, EXTENSIONS, AND APPLICATIONS

C.1 LIKELIHOOD ANALYSIS OF THEORETICAL AND EMPIRICAL GENERALIZATION SCALING LAWS

We hypothesized in the main text that the observed discrepancies in generalization scaling between natural and medical images with respect to intrinsic dataset dimension d_{data} (Fig. 2) were at least partially caused by the notable differences in dataset label sharpness $(K_{\mathcal{F}})$ between these two domains, indicated by our derived generalization scaling law of Equation (2). If we take Eq. (2) as an equality (in other words, a model that can be regressed to the observed generalization data in Fig. 2), we can analyze the likelihood that the observed shift between domains is caused by the scaling law's accounting for $K_{\mathcal{F}}$ by seeing if the likelihood of our scaling law model (Model A) which accounts for $K_{\mathcal{F}}$,

$$y_{\mathbf{A}}(d_{\text{data}}, N, K_{\mathcal{F}}; a) := \log L \simeq -\frac{1}{d_{\text{data}}} \log N + \log K_{\mathcal{F}} + a$$
 (24)

is higher than the likelihood of a model that does not account for $K_{\mathcal{F}}$ (Model **B**),

$$y_{\mathbf{B}}(d_{\text{data}}, N; a) := \log L \simeq -\frac{1}{d_{\text{data}}} \log N + b.$$
 (25)

Here, recall that L is the test loss of a trained network given the intrinsic dimension d_{data} and label sharpness $K_{\mathcal{F}}$ of the network's training dataset (Sec. 3), and N is the size of the training set. Each of the two scaling law models \mathbf{A} and \mathbf{B} will be fit to the observed generalization scaling data D: $D = \{(L; d_{\text{data}}, N, K_{\mathcal{F}})_i\}_{\forall i}$ for model \mathbf{A} and $D = \{(L; d_{\text{data}}, N)_i\}_{\forall i}$ for model \mathbf{B} , using all result data i for a given network architecture (i.e., the datapoints in Fig. 2); the fitted parameters are a and b, for each respective model. We obtained these fitted models using SciPy's curve_fit function (Virtanen et al., 2020), resulting in best-fit parameters of \hat{a} and \hat{b} .

The likelihood ratio between two models is a well-known statistical test for determining the model that better explains the observed data (Vuong, 1989), and is defined by $\mathcal{R}:=p(D|\text{model }\mathbf{A})/p(D|\text{model }\mathbf{B})$. For such regression problems, the likelihood ratio is evaluated as

$$\mathcal{R} = \frac{p(D|\text{model }\mathbf{A})}{p(D|\text{model }\mathbf{B})} = \frac{\exp\left[-\frac{1}{2}\sum_{i}(\log L_{i} - y_{\mathbf{A}}(d_{\text{data},i}, N_{i}, K_{\mathcal{F},i}; \hat{a}))^{2}\right]}{\exp\left[-\frac{1}{2}\sum_{i}(\log L_{i} - y_{\mathbf{B}}(d_{\text{data},i}, N_{i}; \hat{b}))^{2}\right]}.$$
 (26)

Here, $\log \mathcal{R} > 0$ will indicate that model **A** explains the data better, $\log \mathcal{R} < 0$ will indicate that model **B** explains the data better, and $\log \mathcal{R} \approx 0$ indicates that neither model is preferred.

As shown in Table 2, we found that $\log \mathcal{R} > 0$ by a large margin for all network architectures, supporting the importance of accounting for $K_{\mathcal{F}}$ in the scaling law, due to the variability of it across

different domains. These results seem reasonable because as shown in Fig 2, there is a visible separation between the loss curves for the domains of natural and medical images. Allowing the scaling law to account for the label sharpness $K_{\mathcal{F}}$ of the dataset will make it more accurate because different datasets possess different $K_{\mathcal{F}}$ values (Fig. 1), and by Equation (24), different $K_{\mathcal{F}}$ values will move the loss curve up and down.

ResNet-18	ResNet-34	ResNet-50	VGG-13	VGG-16	VGG-19
13.5	7.6	11.7	8.1	10.5	12.3

Table 2: Log-ratio $\log \mathcal{R}$ between (A) the likelihood of the network generalization d_{data} scaling law model that accounts for label sharpness, and (B) the likelihood of the scaling law model that does not, given generalization data observed in our experiments (Fig. 2), for each network architecture.

C.2 EVALUATING A DATASET FROM AN ADDITIONAL DOMAIN

In this section, we extend our analysis to a new dataset from a third domain beyond natural images and radiology images, in order to determine whether our hypotheses extend to other domains (e.g., that dataset label sharpness is related to which domain the dataset is within). We use the ISIC skin lesion image dataset of Codella et al. (2018), which interestingly, has certain characteristics that both natural and radiological images share, such as being RGB photographs (like natural images), and having standardized acquisition procedure and object framing for the purpose of clinical tasks (like radiological images). For all experiments we use the task/labeling for melanocytic nevus detection.

First, we find that ISIC has an intrinsic dimension $d_{\rm data} \simeq 12$ that is in between typical natural image dataset $d_{\rm data}$ values and typical radiology dataset $d_{\rm data}$ values (Fig. 9, left). We similarly see that its label sharpness $\hat{K}_{\mathcal{F}} \simeq 10^{-4}$ is in the upper end of typical natural image dataset $\hat{K}_{\mathcal{F}}$ values, and below all radiology dataset $\hat{K}_{\mathcal{F}}$ (Fig. 9, right). It makes intuitive sense that these intrinsic properties of the ISIC dataset are in between the two domains of natural and radiological images, given the aforementioned characteristics of images from both domains that it possesses.

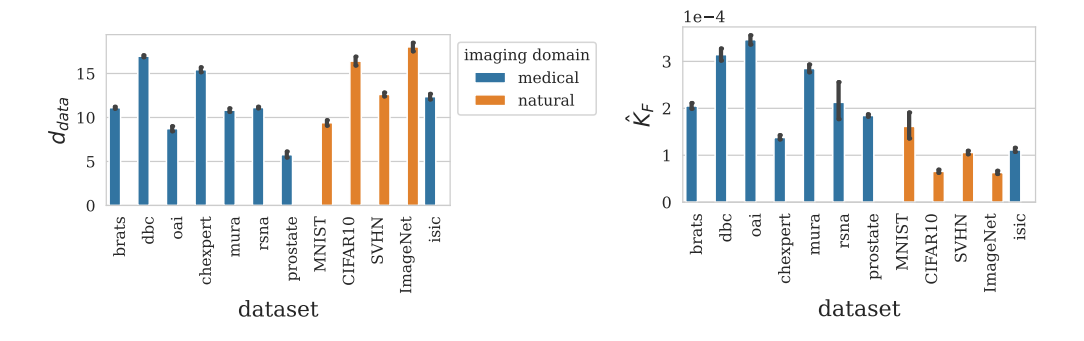


Figure 9: Measured intrinsic dimension ($d_{\rm data}$, left) and label sharpnesses ($\hat{K}_{\mathcal{F}}$, right) of the natural (orange) and medical (blue) image datasets which we analyze (Sec. 4), with the ISIC dataset included on the right of both figures. $d_{\rm data}$ values are averaged over all training set sizes, and $\hat{K}_{\mathcal{F}}$ over all class pairings (Sec. 3.2); error bars indicate 95% confidence intervals.

We next performed the same generalization experiments as in the main text for ISIC, training each network model for the assigned task with N=1750. Given our generalization scaling law of Eq. (2), ISIC having a $K_{\mathcal{F}}$ value between the typical respective values of natural and radiological domains would imply that models trained on the dataset would have test loss values between the models trained on these two domains, given ISIC's $d_{\rm data}$. We see in Fig. 10 that this was indeed the case for all network architectures; the generalization ability of the ISIC models (indicated by purple circles) are between the typical generalization curves of natural image models and radiological image models.

Moreover, the "in-between" $K_{\mathcal{F}}$ of ISIC also implies that models trained on this dataset would be more adversarially robust than the radiological image models (with their high dataset $K_{\mathcal{F}}$ values),

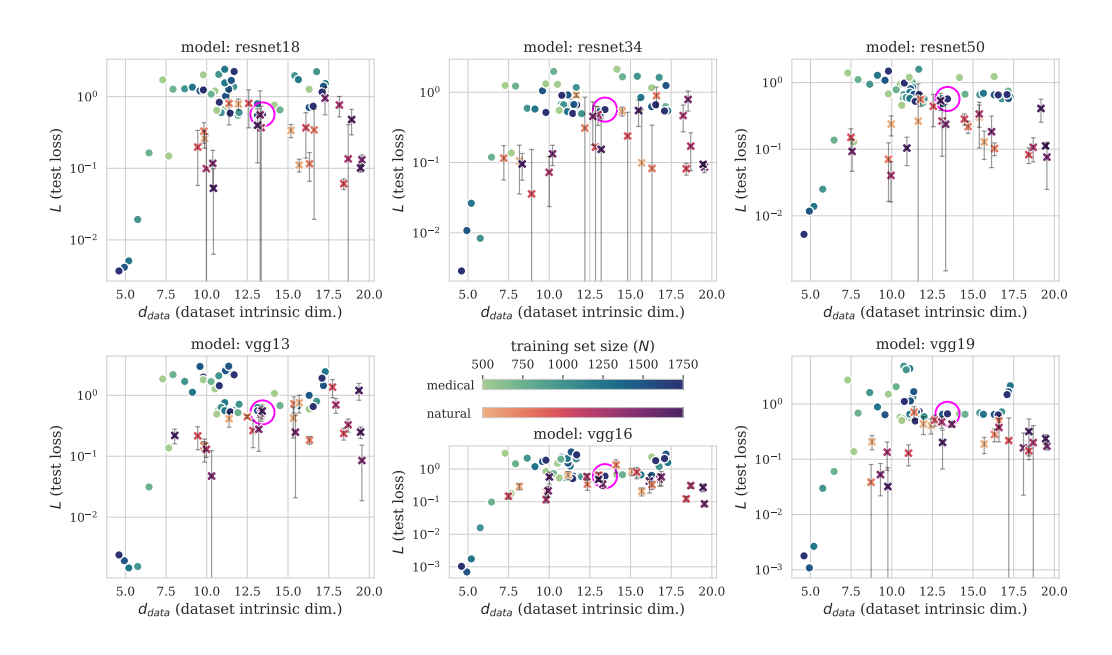


Figure 10: Same as Fig. 2, but with ISIC dataset results added with purple circles.

yet less robust than the natural image models (with their low dataset $K_{\mathcal{F}}$) (Theorem 3). In Fig. 11 we see that this is the case for some network architectures, while for others, ISIC models (purple circles) end up close to the natural image models.

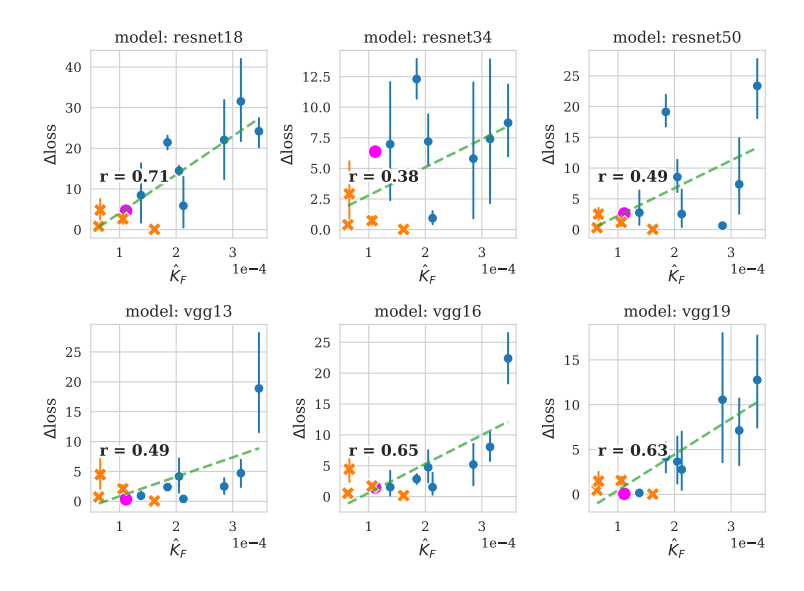


Figure 11: Same as Fig. 3, but with ISIC dataset results added with purple circles.

C.3 PRACTICAL APPLICATION: TASK SELECTION FOR MEDICAL IMAGES

In this section we will demonstrate a practical usage of our formalism. It is common for new medical image datasets to come equipped with many different labels provided by clinical annotators, prior to any attempt to train a model to learn to make such predictions from the data. The question we examine in this section is: given a new dataset with a variety of image labels, which tasks will be easier for a model learn, and which will be harder? This is an important question to guide the model development process of practitioners who wish to take the first steps of training models for

automated diagnosis of a new dataset and/or modality, the answer of which may not be clear solely from the visible image characteristics.

For example, the RSNA-IH-CT dataset (Sec. 4) was annotated with labels for different types of hemorrhages, but some could be easier to detect than others. Consider that we wish to decide whether to train a binary classification model to (1) detect *any* type of hemorrhage out of 5 subtypes or (2) detect a specific type, such as epidural hemorrhage. Naïvely, it may seem that the second task is more specific and therefore may be more challenging, yet if some visual characteristic makes epidural hemorrhages easily noticeable, the first task could be more challenging, as it requires learning to differentiate between (a) healthy cases and (b) each type of hemorrhage. We can get a general idea for the relative difficulty of these two tasks using our derived scaling law, as follows.

Let's say that we wish to estimate which task is likely to be more challenging for a given model to learn by determining which has the higher expected test loss L. Our scaling law (Eq. (2)) estimates that $L \simeq \mathcal{O}(K_{\mathcal{F}}N^{-1/d_{\mathrm{data}}})$, but because the equation is a bound (not an equality), estimating absolute test loss values is not feasible. However, if we instead consider the ratio of test losses for two different possible tasks on the same dataset, a prediction is more tractable. While N and d_{data} are both independent of task choice, the label sharpness $K_{\mathcal{F}}$ (Sec. 3.2) will change depending on the labels assigned to the data for the given task, which can be quickly measured from the dataset without any model training. If we take $K_{\mathcal{F}}^{(1)}$ and $L^{(1)}$ to be the measured label sharpness and expected test loss for the first task (detection of any hemorrhage), respectively, and likewise for $K_{\mathcal{F}}^{(2)}$ and $L^{(2)}$ for the second task (epidural hemorrhage detection), we get that approximately,

$$\frac{L^{(1)}}{L^{(2)}} \approx \frac{K_{\mathcal{F}}^{(1)} N^{-1/d_{\text{data}}}}{K_{\mathcal{F}}^{(2)} N^{-1/d_{\text{data}}}} = \frac{K_{\mathcal{F}}^{(1)}}{K_{\mathcal{F}}^{(2)}},\tag{27}$$

implying that the task with the higher $K_{\mathcal{F}}$ will likely be more challenging for the model (higher test loss L).

To test this, we measured $\hat{K}_{\mathcal{F}}^{(1)}=2.1\pm0.4\times10^{-4}$ and $\hat{K}_{\mathcal{F}}^{(2)}=1.45\pm0.06\times10^{-4}$ for the two respective tasks (95% CI over 25 evaluations of M^2 pairings M=1000, as in Sec. 3.2 and Fig. 1). Although approximate, Eq. (27) indicates that task 2 will be easier. We then trained each of our evaluated models for each of the two tasks, with results shown in Table 3 (N=1750 and all other training details are the same as for the main paper experiments). We see that all models obtained lower test loss on task 2 than on task 1, and similarly obtained higher test accuracy, indicating that task 2 was indeed easier.

	ResNet-18	ResNet-34	ResNet-50	VGG-13	VGG-16	VGG-19	$\hat{K}_{\mathcal{F}}$
Task 1	1.29	1.23	1.03	0.69	0.50	0.51	2.1 ± 0.4
Task 2	0.64	0.66	0.66	0.63	0.62	0.90	1.45 ± 0.06
Task 1	76%	74%	74%	73%	75%	76%	2.1 ± 0.4
Task 2	80%	83%	83%	85%	82%	81%	1.45 ± 0.06

Table 3: **Top section:** Test set **loss** for each model trained on each of the two hemorrhage detection tasks, alongside the measured label sharpness $\hat{K}_{\mathcal{F}}$ for each task (Task 1 is detecting any hemorrhage, Task 2 is detecting epidural hemorrhage). **Bottom section:** Same, but for test set **accuracy**.

Note that Equation (27) is just an approximation, and that tasks with more similar measured $K_{\mathcal{F}}$ values for the same dataset could be harder to distinguish. Of course, this experiment is just an example, and future study with other datasets is warranted.

C.4 EVALUATION AT MUCH HIGHER TRAINING SET SIZES

While many of our datasets do not support going to substantially higher training set sizes than our main experiments' maximum of N=1750 (see Sec. 4), we can still evaluate the generalization scaling of models training on two datasets that do allow for significantly higher N. To this end, we trained each of our six models on the CheXpert medical image dataset and on the CIFAR-10 natural image dataset (for classes 1 and 2) at the highest training set size possible for binary classification on these datasets, N=9250. We would expect from our generalization scaling law (Eq. (2)), that for a fixed dataset (and therefore $d_{\rm data}$ and $K_{\mathcal{F}}$) and architecture, the loss would decrease with higher

N. The results of this are shown in Tables 4 and 5 below; we see that this is indeed the case for all models (lower loss for higher training set size). We also see that the general trend of the natural image models having much lower loss than the medical image models is maintained, even though these two datasets have similar intrinsic dimensions ($d_{data} \simeq 15-17$).

N	ResNet-18	ResNet-34	ResNet-50	VGG-13	VGG-16	VGG-19
9250	0.1660	0.1821	0.1179	0.1086	0.1045	0.0828
1000	0.5312	0.7402	0.5128	0.9764	0.6001	0.3974

Table 4: Test losses for models trained on CIFAR-10 binary classification for high training set size N = 9250 compared to those trained on N = 1000.

N	ResNet-18	ResNet-34	ResNet-50	VGG-13	VGG-16	VGG-19
9250	0.7712	0.6370	0.6789	0.6014	0.6014	0.6016
1000	1.3479	0.7894	0.9793	0.6700	0.7409	0.6806

Table 5: Test losses for models trained on CheXpert binary classification for high training set size N=9250 compared to those trained on N=1000.

C.5 DEPENDENCE OF NETWORK PERFORMANCE ON IMAGE RESOLUTION

It seems plausible that training a network to perform certain medical image binary classification tasks would be difficult at low image resolutions, due to the visual similarity of positive and negative images for some tasks (as any opposed to the typically low visual similarity of images from different classes in natural image datasets). To test this, we trained a ResNet-18 on each medical image dataset (with N=1750 and all other training settings at their defaults) over a wide range of image resolutions (square image sizes of [32,64,128,256,512]), to see if the test accuracy was smaller for low resolutions. The results are shown in Fig. 12, and surprisingly, there is little performance drop for small resolutions. This may actually make sense, considering datasets like MedMNIST (Yang et al., 2023), where training for a wide variety of medical image classification tasks is possible even at 28×28 resolution. Of course, this would probably not be the case for more fine-grained tasks such as semantic segmentation.

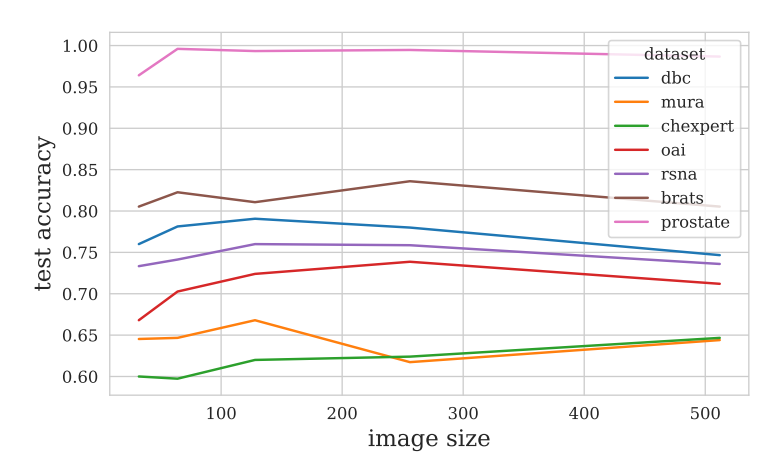


Figure 12: Dependence of network performance on image size for different medical image classification datasets (ResNet-18, training set size of 1750).

D ADDITIONAL VISUALIZATIONS

D.1 EXAMPLE ADVERSARIAL ATTACKS ON MEDICAL IMAGES

We show example attacked medical images for each dataset in Fig. 13.

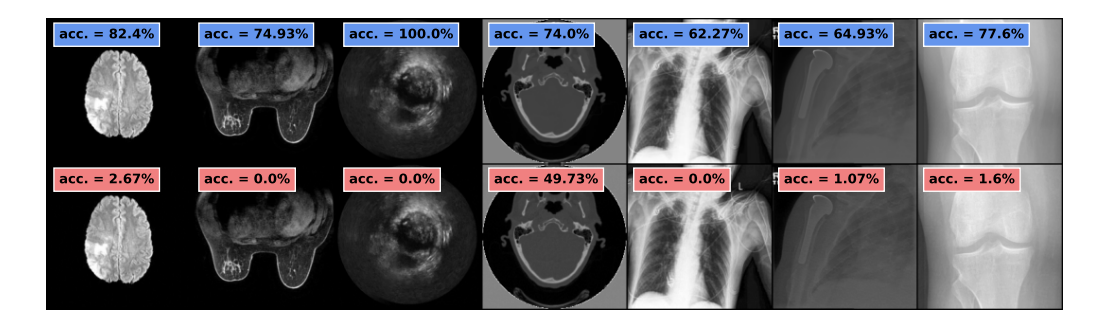


Figure 13: Susceptibility of medical images to adversarial attack. Top row: test set prediction accuracy of models trained on each medical image dataset for its corresponding diagnostic task (Sec. 4), with example test images shown. Bottom Row: accuracies after each test set was attacked by FGSM ($\epsilon=2/255$), with example attacked images shown. The models are ResNet-18s with training set sizes of N=1750.

E MAIN RESULTS WITH OTHER METRICS

In this section we will show our main results but with other metrics for generalization, adversarial robustness, and/or intrinsic dimensionality.

E.1 GENERALIZATION SCALING WITH $d_{ m data}$ AND $d_{ m repr}$

Continuation of Sec. 5.1. In Fig. 14 we show the scaling of test *accuracy* with intrinsic dataset dimension $d_{\rm data}$, using the default MLE estimator (Sec. 3.1). In Figs. 15 and 16 we show the scaling of test loss and accuracy, respectively, but instead using TwoNN (Sec. 3.1) to estimate $d_{\rm data}$.

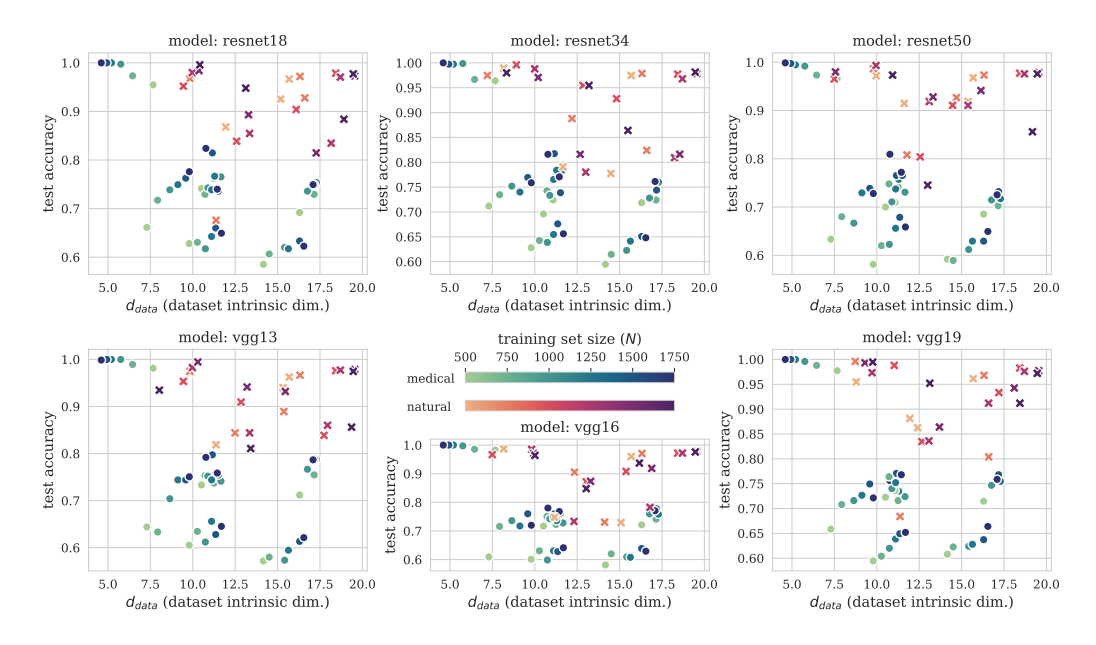


Figure 14: Scaling of test accuracy/generalization ability with training set intrinsic dimension (d_{data}) for natural and medical datasets.

Continuation of Sec. 7. Next, in Fig. 17 we show the scaling of test *accuracy* with learned representation intrinsic dimension d_{repr} , using the default TwoNN estimator (Sec. 3.1). In Figs. 18 and 19 we show the scaling of test loss and accuracy, respectively, but instead using MLE (Sec. 3.1) to estimate d_{repr} .

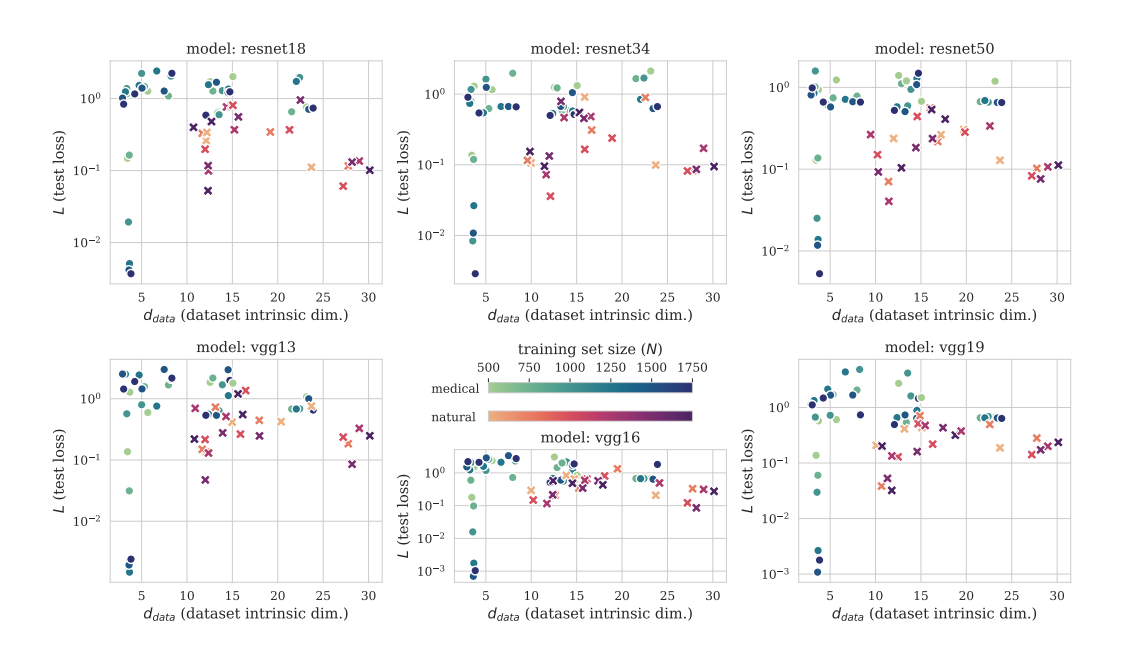


Figure 15: Scaling of log test loss/generalization ability with training set intrinsic dimension ($d_{\rm data}$) for natural and medical datasets, with $d_{\rm data}$ computed via TwoNN (Facco et al., 2017).

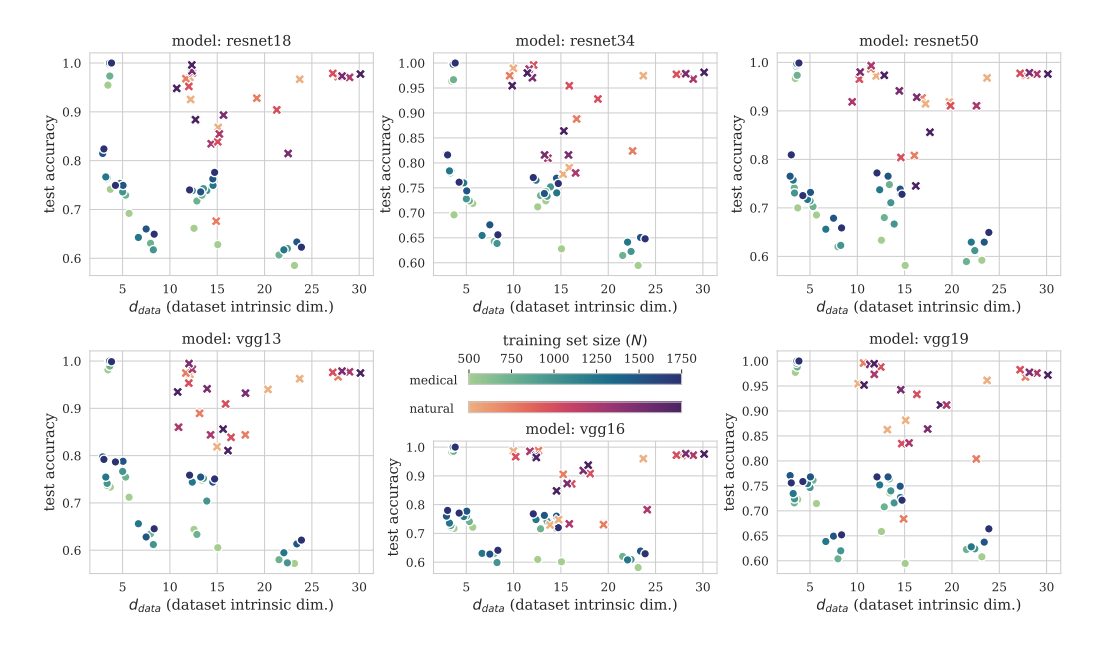


Figure 16: Scaling of test accuracy/generalization ability with training set intrinsic dimension ($d_{\rm data}$) for natural and medical datasets, with $d_{\rm data}$ computed via TwoNN (Facco et al., 2017).

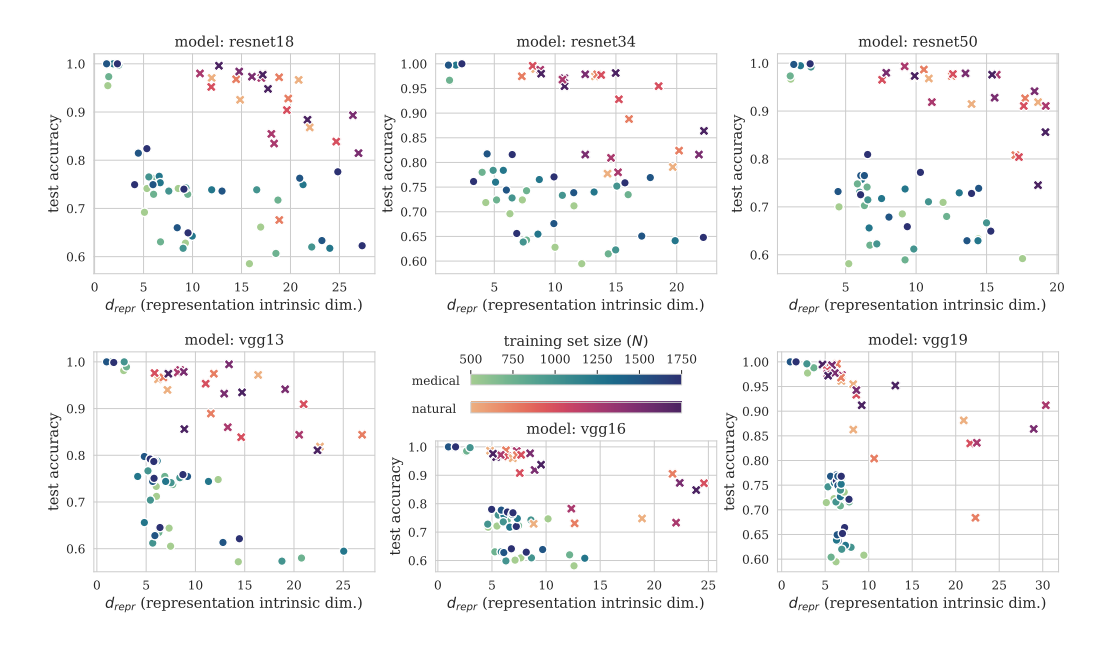


Figure 17: Scaling of test accuracy/generalization ability with the intrinsic dimension of final hidden layer learned representations of the training set (d_{repr}) for natural and medical datasets.

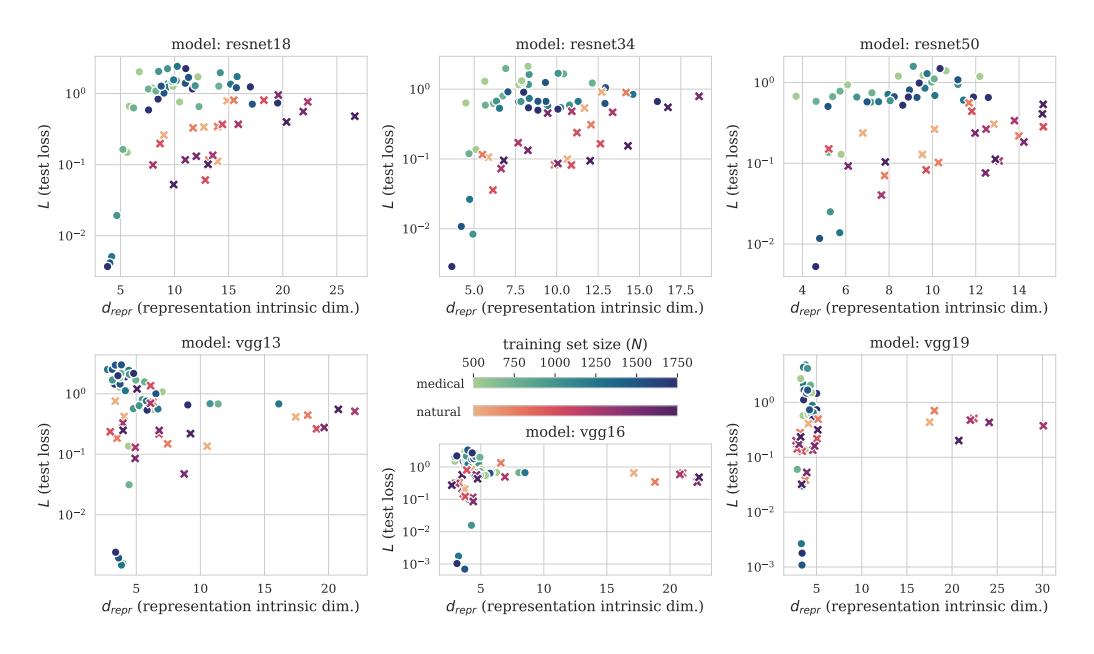


Figure 18: Scaling of log test loss/generalization ability with the intrinsic dimension of final hidden layer learned representations of the training set (d_{repr}) for natural and medical datasets, with d_{data} computed via MLE (Sec. 3.1).

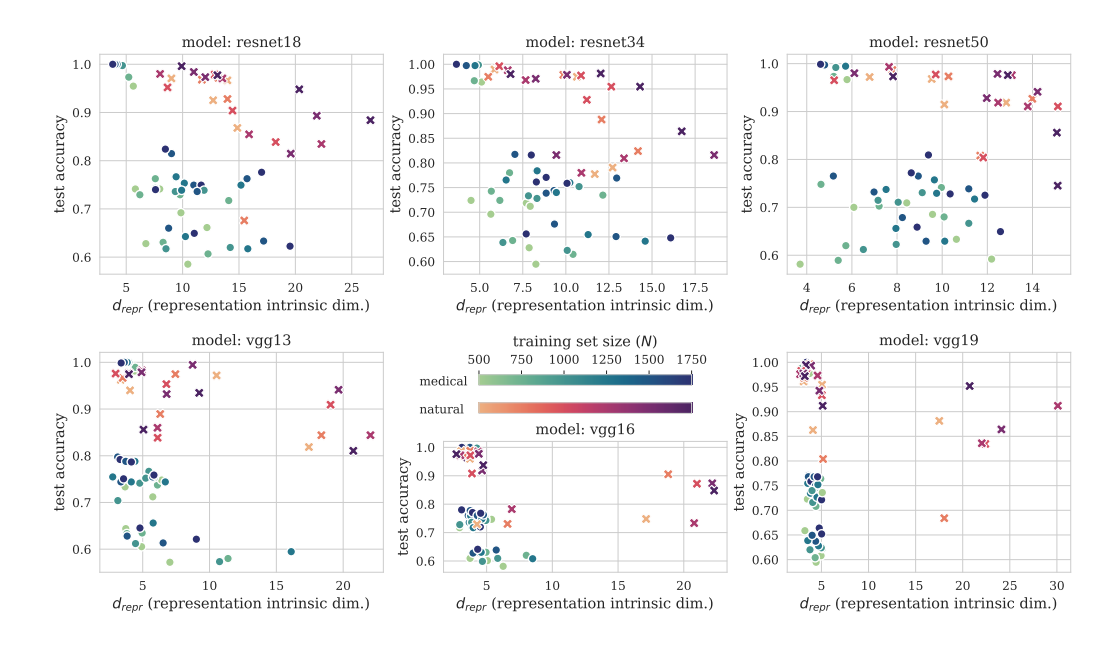


Figure 19: Scaling of test accuracy/generalization ability with the intrinsic dimension of final hidden layer learned representations of the training set (d_{repr}) for natural and medical datasets, with d_{data} computed via MLE (Sec. 3.1).

E.2 BOUNDING HIDDEN REPRESENTATION INTRINSIC DIMENSION WITH DATASET INTRINSIC DIMENSION

In Fig. 20 we show the $d_{\rm data}$ vs. $d_{\rm repr}$ results as in Fig. 5, but with dimensionality estimates computed with TwoNN instead of MLE (Sec. 3.1).

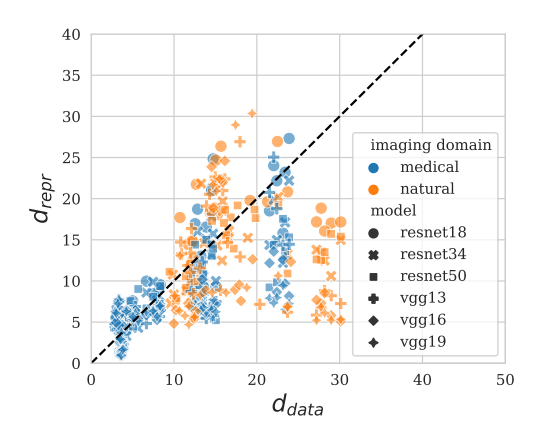


Figure 20: Training dataset intrinsic dimension d_{data} vs. learned representation intrinsic dimension d_{repr} , both computed using TwoNN instead of MLE (Sec. 3.1). Each point corresponds to a (model, dataset, training set size) combination.

E.3 Adversarial Robustness scaling with $\hat{K}_{\mathcal{F}}$

Continuation of Sec. 6. In Figs. 21, 22 and 23, we show the scaling of test loss penalty due to FGSM adversarial attack with respect to measured dataset label sharpness $\hat{K}_{\mathcal{F}}$, for attack ϵ of 1/255, 4/255, and 8/255, respectively. In Figs 24, 25, 26 and 27 we instead show the scaling of test *accuracy* penalty, for each FGSM attack ϵ of 1/255, 2/255, 4/255, and 8/255, respectively.

Finally, in Tables 6 and 7 we report per-domain correlations of loss penalty and dataset $K_{\mathcal{F}}$, for medical images and natural images respectively.

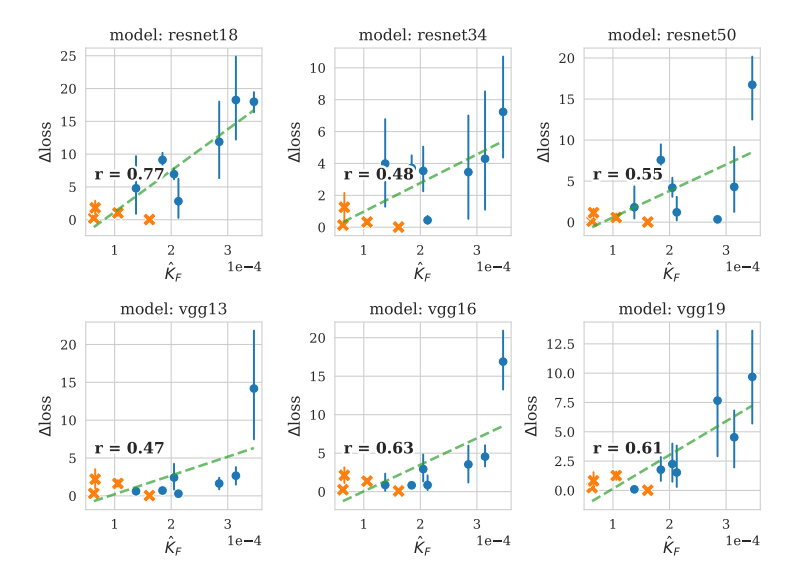


Figure 21: Scaling of test set loss penalty due to $\epsilon=1/255$ FGSM adversarial attack with dataset label sharpness $K_{\mathcal{F}}$ for natural (orange) and medical (blue) datasets.

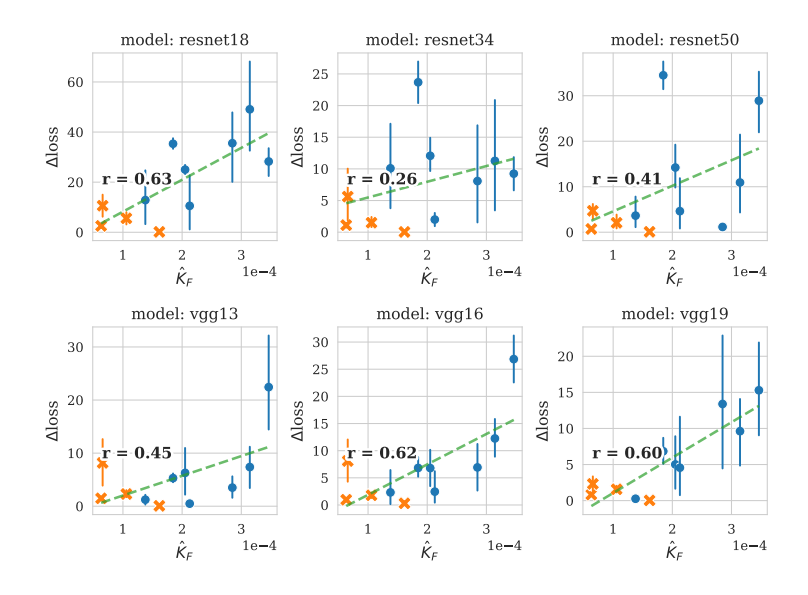


Figure 22: Scaling of test set loss penalty due to $\epsilon=4/255$ FGSM adversarial attack with dataset label sharpness $K_{\mathcal{F}}$ for natural (orange) and medical (blue) datasets.

F TRAINING AND IMPLEMENTATIONAL DETAILS

This section provides training and implementation details beyond that of Sec. 4. We train all models with a binary cross-entropy loss function, optimize by Adam (Kingma & Ba, 2015) with a weight decay strength of 10^{-4} for 100 epochs. We use learning rates of 10^{-3} for ResNet models on all datasets, and 10^{-4} for VGG models on all datasets except SVHN, which required 10^{-6} to avoid loss divergence. ResNet-18, -34 and -50 models were trained with batch sizes of 200, 128, and 64, respectively, and 32 for all VGG models. We do not use any training image augmentations beyond

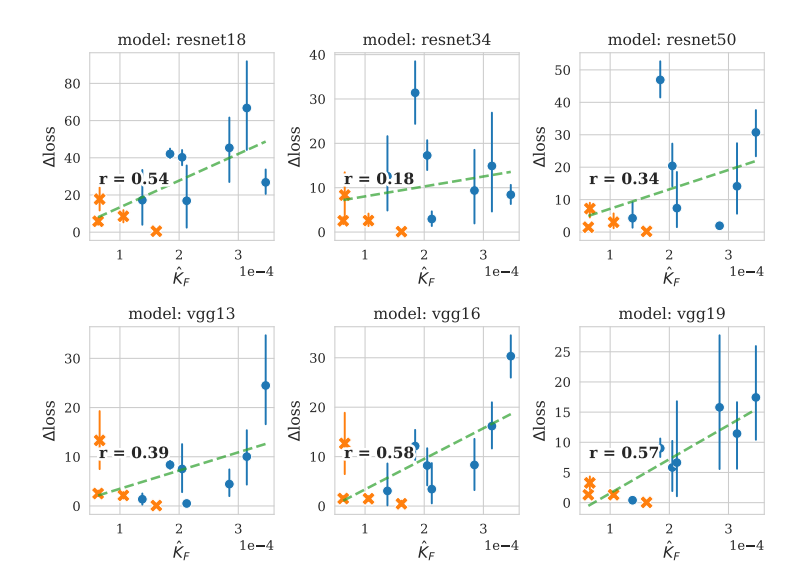


Figure 23: Scaling of test set loss penalty due to $\epsilon=8/255$ FGSM adversarial attack with dataset label sharpness $K_{\mathcal{F}}$ for natural (orange) and medical (blue) datasets.

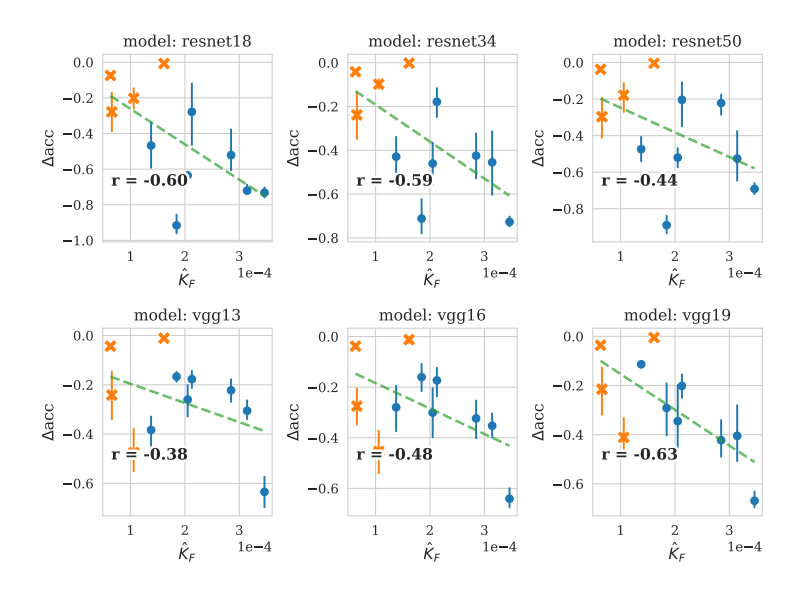


Figure 24: Scaling of test set accuracy penalty due to $\epsilon=1/255$ FGSM adversarial attack with dataset label sharpness $K_{\mathcal{F}}$ for natural (orange) and medical (blue) datasets.

Atk. ϵ	RN-18					V-19
1/255	0.67	0.26	0.43	0.55	0.69	0.6
2/255	0.53	0.01	0.28	0.57	0.71	0.57
4/255	0.41	-0.16	0.14	0.56	0.7	0.53
8/255	0.31	-0.23	0.04	0.56	0.66	0.49

Table 6: Pearson correlation r between test loss penalty due to FGSM attack and dataset label sharpness $\hat{K}_{\mathcal{F}}$, over all **medical image** datasets and all training sizes. "RN" = ResNet, "V" = VGG.

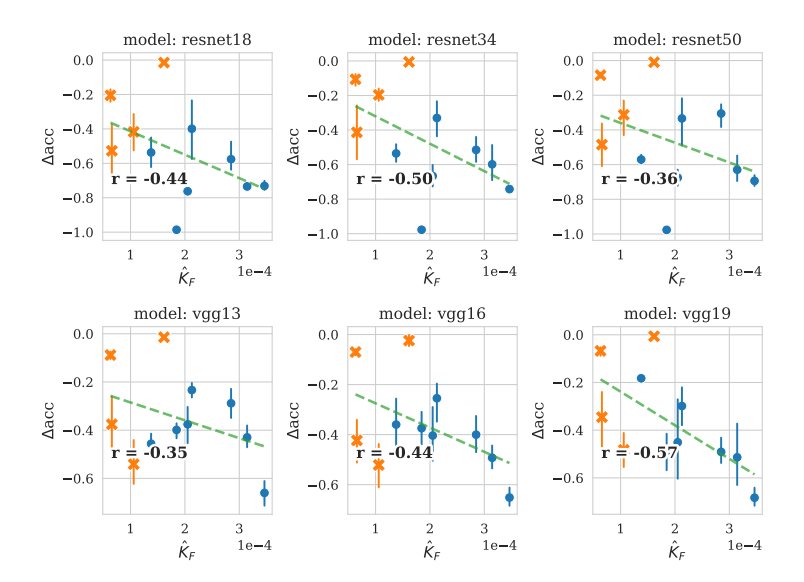


Figure 25: Scaling of test set accuracy penalty due to $\epsilon=2/255$ FGSM adversarial attack with dataset label sharpness $K_{\mathcal{F}}$ for natural (orange) and medical (blue) datasets.

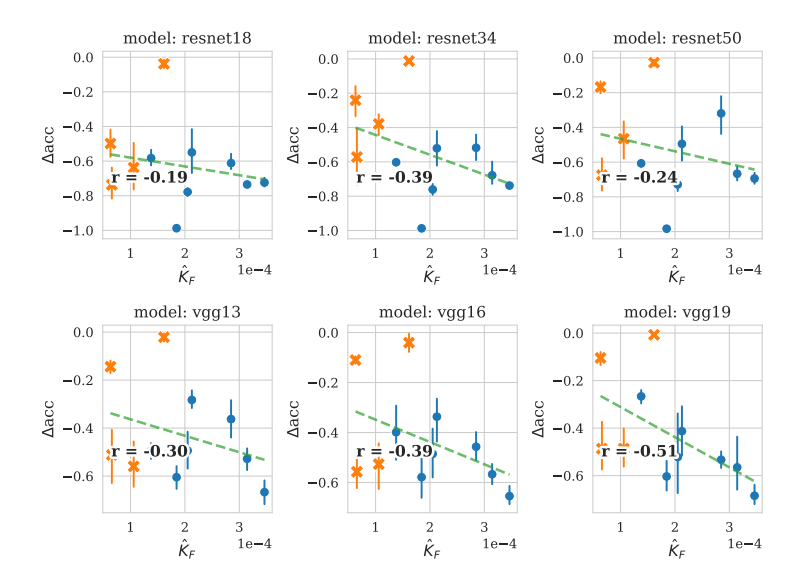


Figure 26: Scaling of test set accuracy penalty due to $\epsilon=4/255$ FGSM adversarial attack with dataset label sharpness $K_{\mathcal{F}}$ for natural (orange) and medical (blue) datasets.

	RN-18					
1/255	-0.39	-0.37	-0.39	-0.36	-0.38	-0.24
2/255	-0.42	-0.37	-0.41		-0.41	
	-0.49			-0.47	-0.43	-0.53
	-0.58			-0.5		

Table 7: Pearson correlation r between test loss penalty due to FGSM attack and dataset label sharpness $\hat{K}_{\mathcal{F}}$, over all **natural image** datasets and all training sizes. "RN" = ResNet, "V" = VGG.

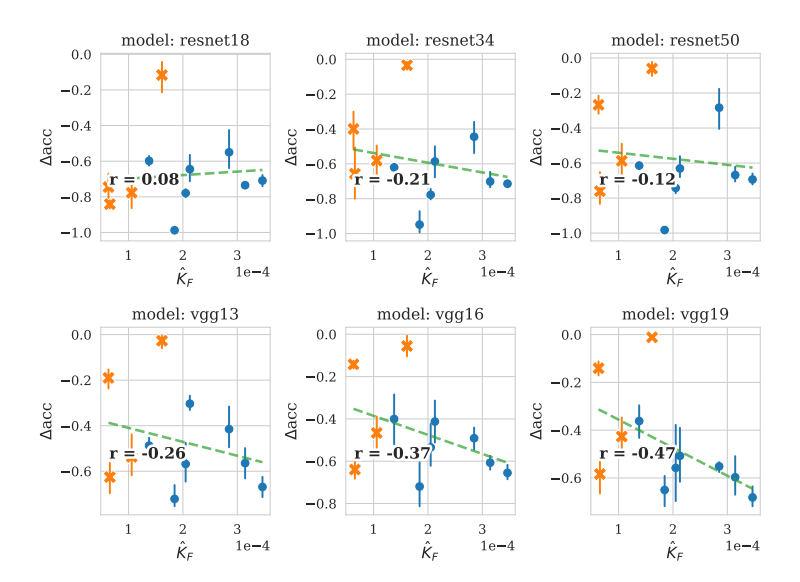


Figure 27: Scaling of test set accuracy penalty due to $\epsilon = 8/255$ FGSM adversarial attack with dataset label sharpness $K_{\mathcal{F}}$ for natural (orange) and medical (blue) datasets.

resizing to 224×224 and linear normalization to [0,1]. We perform all experiments on a 48 GB NVIDIA A6000.

G MEDICAL IMAGE DATASET DETAILS

This section goes into full detail into the binary classification task definitions for each medical image dataset, beyond what is mentioned in Section 4. We follow the same task definitions for the medical image datasets as in Konz et al. (2022). Specifically:

- For OAI (Tiulpin et al., 2018), we use the screening packages 0.C.2 and 0.E.1, and define a negative class of X-ray images with Kellgren-Lawrence scores of 0 or 1, and a positive class of images with scores of 2+.
- For DBC (Saha et al., 2018), we use fat-saturated breast MRI slices. Slice images with a tumor bounding box label are positive, and any slice at least 5 slices away from a positive slice is negative.
- We use the same slice-labeling procedure as DBC for BraTS (Menze et al., 2014), for glioma labels in T2 FLAIR brain MRI slices.
- For Prostate MRI (Sonn et al., 2013), we use slices from the middle 50% of each MRI volume. Slices are labeled as negative if the volume's cancer risk score label is 0 or 1, and positive for 2+.
- For brain CT hemorrhage detection in RSNA-IH-CT (Flanders et al., 2020), we detect for *any* type of hemorrhage.